AFRL-RQ-WP-TR-2022-0052

PROBABLISTIC BARELY VISIBLE IMPACT DAMAGE (BVID) RISK ASSESSMENT TOOL

Paul Davidson

University of Texas at Arlington

APRIL 2022

FINAL REPORT

NOTICE AND SIGNATURE PAGE

Using Government drawings, specifications, or other data included in this document for any purpose other than Government procurement does not in any way obligate the U.S. Government. The fact that the Government formulated or supplied the drawings, specifications, or other data does not license the holder or any other person or corporation; or convey any rights or permission to manufacture, use, or sell any patented invention that may relate to them.

This paper was cleared for public release by AFRL Public Affairs, AFRL/PA and is available to the general public, including foreign nationals.

Copies may be obtained from the Defense Technical Information Center (DTIC) (https://discover.dtic.mil).

AFRL-RQ-WP-TR-2022-0052 has been reviewed and is approved for publication in accordance with assigned distribution statement.

This paper is published in the interest of scientific and technical information exchange and its publication does not constitute the Government's approval or disapproval of its ideas or findings.

REPORT DOCUMENTATION PAGE

Form Approved
OMB No. 0704-0188

1. REPORT DATE *(DD-MM-YY)*	2. REPORT TYPE	3. DATES COVERED *(From - To)*
30 April 2022	FINAL REPORT	30 Jul 2019 – 30 June 2022

4. TITLE AND SUBTITLE
PROBABLISTIC BARELY VISIBLE IMPACT DAMAGE (BVID) RISK ASSESSMENT TOOL

5a. CONTRACT NUMBER

5b. GRANT NUMBER
FA8650-19-2-2213

5c. PROGRAM ELEMENT NUMBER

6. AUTHOR(S)
Paul Davidson (PI)
Andrew Seamone
Anthony Waas

5d. PROJECT NUMBER

5e. TASK NUMBER

5f. WORK UNIT NUMBER
Q28W

7. PERFORMING ORGANIZATION NAME(S) AND ADDRESS(ES)
University of Michigan,
503 Thompson St,
Ann Arbor, MI

8. PERFORMING ORGANIZATION REPORT NUMBER

9. SPONSORING/MONITORING AGENCY NAME(S) AND ADDRESS(ES)
Air Force Research Laboratory
Aerospace Systems Directorate
Wright-Patterson Air Force Base, OH 45433-7541
Air Force Materiel Command
United States Air Force

10. SPONSORING/MONITORING AGENCY ACRONYM(S)
AFRL/RQVS

11. SPONSORING/MONITORING AGENCY REPORT NUMBER(S)

12. DISTRIBUTION/AVAILABILITY STATEMENT
DISTRIBUTION STATEMENT A. Approved for public release. Distribution is unlimited.
AFRL-2023-1285; Cleared 03/16/2023.

13. SUPPLEMENTARY NOTES

14. ABSTRACT

Impact damage of laminated composite structures continues to be a challenging problem. The complexity of damage morphology, the sequence of damage events, and multiple damage modes pose significant challenges when it comes to design for damage tolerance. In an effort to reduce some of the complexity, a systematic experimental study was conducted to understand the sequence of damage during impact of a thin and thick composite plates. Varying configurations of carbon fiber reinforced epoxy composite panels were impacted with increasing impact energies. Digital image correlation (DIC) using high speed camera was performed to measure plate deflection and strain evolution during the impact event. Detailed post impact measurement and imaging were conducted to quantify the extent of damage and delamination. Compression after impact (CAI) tests were conducted to ascertain the post impact compressive load carrying capability of the panel. The results of the experiments indicate a sequence of damage from back surface splitting, delamination and then impact surface compressive failure. Correlations were also found between impact energies, panel configuration and damage type and morphology. The extent of impact damage as well as the compressive strength knockdown is very different between thin composites and thick composites. The data thus generated is useful for validating computational models for impact damage and CAI. An approach to performing such validation is also provided in this study.

15. SUBJECT TERMS

16. SECURITY CLASSIFICATION OF:			17. LIMITATION OF ABSTRACT:	18. NUMBER OF PAGES	19a. NAME OF RESPONSIBLE PERSON (Monitor)
a. REPORT	b. ABSTRACT	c. THIS PAGE			Padmasiri V Ranatunga
Unclassified	Unclassified	Unclassified	SAR	56	19b. TELEPHONE NUMBER *(Include Area Code)* (937) 656-8809

TABLE OF CONTENTS

LIST OF FIGURES

Figure **Page**

LIST OF TABLES

Table **Page**

1. SUMMARY

The goal of this SIRCA program was to systematically study the sequence of damage and post-damage load carrying capability of composite laminates under Barely Visible Impact Damage (BVID) regime. Results obtained from this program will have direct influence on the damage tolerance and aircraft sustainment design practice with Airforce and airframers.

Five composite configurations relevant to current aircrafts were selected for the program. The configuration ranged from thin composite used in fuselage sections and thick composite used in wing section of aircraft. Panels were manufactured at AFRL and sent to University of Michigan for test and analysis. Sample panel of selected composite configurations were impacted at increasing energy levels under controlled boundary conditions to ensure repeatability and accurate damage measurements. Detailed post impact measurements were conducted to characterize and quantify every aspect of impact damage, from dent depth to through thickness delamination. Careful analysis of impact experiments was conducted to determine damage sequence. Threshold energies for backsplit, delamination and surface damage were quantified. Damage size and morphology was characterized using ultrasound scans. Influence of damage on the structural performance of composite was characterized by conducting Compression After Impact (CAI) experiments. Compression strength knockdowns were correlated with impact energy and damage size.

In addition to experimental work, novel tool was developed to automate impact damage model generation. The tool can be used to efficiently generate complete BVID virtual experimental model to be used with Finite Element Analysis (FEA). Careful study was also conducted to measure sensitivity of damage parameters used on the results of the model.

The information generated in this program has also created a unique database of damage pattern, compression strength knockdown and complete sequence of failure for Airforce relevant composite laminate stack up and material system. The database generated can be used in future to inform design and analysis. Additionally, it can also be used for risk identification while performing ultrasound scan of composite structures at maintenance yards. Furthermore, an automated mesh generation and analysis tool was also developed to provide Airforce analyst a high fidelity virtual BVID and CAI method for impact and post-impact risk assessment.

Keywords: Low Velocity Impact, Compression After Impact, Damage, Delamination

2. INTRODUCTION

2.1. Background

Carbon Fiber Reinforced Polymer Composites (CFRP) have been increasingly used in aircraft structural components due to advantages in their strength-to-weight ratio and ability to meet complex design criteria. However, an application constraint of CFRPs arises from their strength reduction due to low-velocity impacts (LVI). These impacts can occur as a result of a dropped tool or equipment during manufacturing and maintenance. LVI events are hazardous to composites because they often generate Barely Visible Impact Damage (BVID), where a composite component suffers damage that is not detectable on the impacted surface. In these instances, impact-induced delaminations develop between laminae. This damage can be detrimental to a composite's peak load-carrying capability when the delaminations become sufficiently large.

LVI events have been studied experimentally using drop towers as standardized in ASTM D7136 [1]. This experiment produces impact damage for composites in an unloaded state. This applies to composites that suffer BVID due to tool drops and errors during the manufacture and assembly of aircraft. Other studies have also investigated the impact damage of specimens loaded in compression for other applications, such as debris striking an aircraft wing during landing [2]. The behavior of damage and compression load-carrying capability differs between these loading cases. While this standard describes the impact conditions for a 152.4 mm by 101.6 mm panel, studies have been performed on larger-sized panels using a similar approach [3]. Previous studies have shown the use of high-frame-rate 3D Digital Image Correlation (DIC) to analyze the in situ response of impact events [4–7].

Interlaminar delaminations can be inspected through various Nondestructive Inspection (NDI) techniques. NDI is very useful when evaluating damaged composites because it allows for subsequent testing to be performed on a damaged test specimen. Additionally, NDI serves as a valuable tool for inspection and maintenance tasks for in-service composite structures where the strength can be evaluated based on the investigated damage. Previous studies have evaluated the effectiveness of several NDI techniques, including the tap test, PC swept/RF, ultrasonic testing, shearography, and thermography [8, 9]. Of these discussed methods, Ultrasonic Testing (UT) was the most effective tool for observing delamination. Another effective and accurate method for NDI is X-ray Computed Tomography (CT). X-ray CT has been used in previous impact damage inspection studies [3, 4]. While it can render accurate scans of damage within a composite, it can be very time-consuming and expensive and limits the size of a specimen for investigation. Until recently, UT had similar limitations to X-ray CT in that UT required immersion scanning and was also limited by portability and specimen size [10]. Recently, UT has emerged as an efficient tool to identify the size of delamination within a composite. The advantage of modern UT scanners comes from their portability and ability to accurately measure the extent of delamination in very little time. A limitation of UT is its inability to detect damage beyond the first detection of damage at a location. This generates what is known as a ’shadow region’ beneath the first observed instances of delamination. While UT provides only partial information on the delaminated regions within the composite, it can accurately identify the delamination area's overall size (footprint).

The transition from BVID to Visible Impact Damage (VID) can be challenging to quantify. The detectability of VID can be defined as the residual depth of the depression formed by the impactor after the impact event, expressed as the maximum distance in a direction normal to the face of the

specimen from the lowest point in the dent to the plane of the undisturbed impact surface [11]. To quantify this description, a dent depth of 300 microns is assigned to this transition [11–13]. It is important to note that this definition is currently used in the industry but has its limitations in accurately defining BVID. A study by Talreja showed that the dent depth measurement for impacted carbon/epoxy composites can vary based on the thickness of the laminate, and that setting a dent depth measurement as the threshold for BVID may not accurately describe the detectability of the damage [12]. Even if a definition of BVID that encompasses a range of laminate thicknesses is introduced, its value with respect to identifying the structural response in compression of an impact-damaged panel may not be straightforward. It is noted that the dent depth value of 300 microns is used in this study because it separates both the 16 and 24-ply laminates into BVID and VID categories. In the visible instances, top surface fiber and matrix failure are also observed, which contribute to a larger dent depth.

LVI events can cause intra-ply damage, such as fiber failure and matrix failure, and inter-ply damage, such as delamination between laminae. These failure mechanisms can significantly reduce the Compression After Impact (CAI) strength of a composite [14–17]. In extreme cases, the compressive strength of a composite can be knocked down to 30 percent of its undamaged state with no indication of damage on the impacted surface [18]. Because of this, damage tolerance is a very significant consideration for the design and use of composite structures. A CAI experiment is standardized in ASTM D7137 [19]. There are much aerospace uses for both thin and thick composites. Typically, composites with a thickness greater than 3 mm are designed not to buckle globally, whereas thinner composites are more likely to [20]. When delaminations are present, local buckling may occur. There have been several studies on the behavior of thin composites subject to impact damage, mostly within the range of 2-3 mm in thickness [12, 21–27]. Thin composite panels are of great interest due to aerospace applications such as fuselages of an aircraft, cryogenic tanks of reusable launch vehicles, and fan blades of a turbojet engine [20]. This requires consideration for the effect impact damage has on the compressive response of thin composites, including final failure [28].

A computational model for BVID using Finite Elements (FE) is also presented in this report. The model is useful for accurately capturing the BVID response of the composite and correctly predicting the extent of inter-ply delaminations as well as intra-ply damage in the form of fiber and matrix failure. The development of this model requires an extensive data set to predict these features for different impact energies, stacking sequences, and thicknesses. An accurate model would be able to replace the need for large numbers of tests leading to savings in cost and time [29].

Several challenges arise while modeling the impact response of composites. These include the modeling of the force response of the impact event, the extent of delamination (the footprint), and fiber and matrix damage throughout the composite. Two finite element-based effective methods of modeling the extent of delamination in an impacted composite are through cohesive contact, as shown in [4, 30], and cohesive elements, as shown in [31, 32]. Previous studies suggest that experimental results are best matched using the cohesive contact modeling approach for delamination [6, 33]. This study utilized a fiber-aligned mesh to increase the fidelity of the model [4, 34, 35]. Other studies utilize an unstructured mesh which can require fewer inputs and run more efficiently [15, 30].

2.2. Scope

This study aims to understand the initiation, progression, and sequence of failure events in composite laminates of varying lamination stack-up and thickness under BVID and CAI. A systematic and detailed test campaign was conducted wherein new fixtures were developed to ensure repeatable tests. Furthermore, detailed post-test measurements were made for impact dent depth, damage, and delamination. In addition to this overall goal, an understanding of the order of failure events during impact is obtained, and a relationship between impact energy and observed UT de-lamination is developed. Finally, the information gained from the extensive data set is utilized in refining the computational model to predict the extent of delamination accurately.

The report is structured as follows; section 3.1 provides the details for the experimental setup, which includes sample preparation; section 3.2 details the experimental protocol; section 4.1 discusses the impact test results; section 4.2 details the post-impact measurement; section 4.3 has the results for compression after impact. Section 4.4 analyses the results, followed by section 4.5 with computational modeling. The final section has the conclusions.

3. METHODS, ASSUMPTIONS, AND PROCEDURES

3.1. Experimental setup

3.1.1. Sample preparation

Composite laminated plates made with IM7/977-3 material system, with stacking sequences (Table 1) representing typical stack-up used in aircraft. As can be seen the laminates are symmetric but are not quasi-isotropic. Samples were tagged based on their manufacture plate and specimen ID for each stack up. The panels were also inspected for manufacturing defects using a portable ultrasound inspection device, DolphiCam2. Table 2, details the total number of specimens used for impact and compression after impact (CAI) tests. For both impact and CAI experiments, a speckle pattern was spray painted for 3D Digital Image Correlation (DIC) measurements on each specimen.

Table 1: Composites in Study

Sample tag	Stacking sequence	Panel thickness (mm)
F16	$[45, 0, -45, 0, 45, 90, -45, 0]_s$	2.064
F24	$[45, -45, 0, 90, 0, 45, 90, 45, 0, -45, 0, 45]_s$	3.096
WL40	$[45, 0, -45, 0, 45, 90, 0, -45, 90, 45, 0, 45, -45, 0, 0, 45, 0, 0, -45, 90]_s$	5.160
WU48	$[45, -45, 0, 90, 0, -45, 0, 45, 0, 90, 45, -45, 0, 45, 0, 90, 0, -45, 0, 45, -45, 90, -45, 45]_s$	6.192

WL56	$[45, 0, -45, 45, 0, 45, 90, -45, 0, 0, 45, 0, -45, 0, 45, 90, -45, 0, 0, 45, 90, -45, 0, -45, 45, 0, -45, 0]_s$	7.224

Table 2: Number of specimens for each experiment

Sample tag	Impacted panel	Pristine CAI	Damaged CAI
F16	25	2	10
F24	24	2	11
WL40	10	1	6
WU48	10	1	6
WL56	9	1	6

3.1.2. Impact setup

Impact testing was performed according to ASTM D7136 with an impact fixture adapted to test 178mm x 178mm panels [1]. The panel was secured between the top and bottom roller support plates of the impact fixture as shown in figure 1. These supports provided a 152 mm x 152 mm (6” x 6”) supported boundary and were secured with four steel bolts. An Instron CEAST 9350 drop tower was used to drop a steel hemispherical impactor onto the top face of composite panel. The steel impactor of 25.4 mm (1”) diameter, and a total drop mass of 8.53 kg was used for each

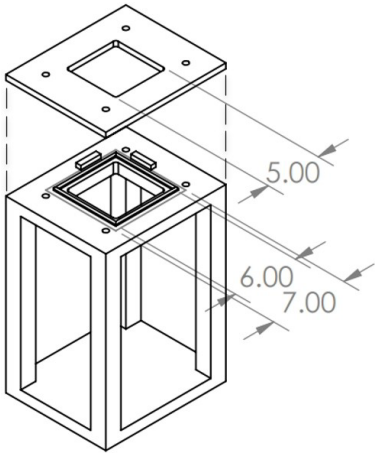

Figure 1 Impact fixture

experiment. The impact energy was varied between tests by adjusting the drop height of the impactor, which ultimately controlled the velocity of the impactor as it reached the top surface of the composite. A pressurized arm automatically activated to catch the impactor after the initial

impact, ensuring that the impactor only struck the composite once. Two Photron Fastcam SA-X high-speed 1024 x 1024 pixel cameras captured the bottom surface of the composite at 12,500 frames per second via a front-surfaced mirror placed underneath the sample. The mirror was angled at 45 degrees relative to the surface of samples and was bolted into the base of the steel impact fixture. An optical sensor was used to trigger the Instron and the high-speed cameras to start recording simultaneously, at the time of impact.

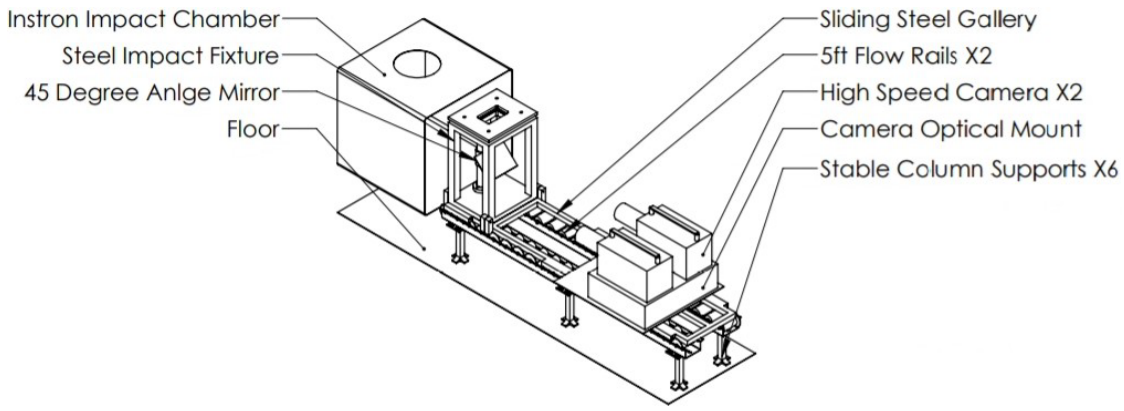

Figure 2 Impact test rig

To ensure impact testing procedure accuracy, efficiency, and repeatability, an impact rig was assembled as shown in figure 2. Cameras were fixed on an optical mount on steel plate to hold the camera system in place. The plate was fixed onto a steel frame that slide along two parallel flow rails towards and away from the steel impact fixture. The flow rails were supported by six steel floor supports with adjustable heights to ensure that the flow rails were parallel and level across their length.

DIC analysis were performed using Aramis software. A standard 13-position calibration was performed, using a calibration panel, and Aramis DIC software. The setup provided an acceptable calibration deviation of 0.01-0.04 pixels [36]. The angle between the two cameras was fixed at 25◦ which provided the best calibration. The brightness of the illumination was adjusted such that the pixel intensity of the white spot was at least 100 units larger than the black background [36], to ensure good DIC image quality. Once a successful calibration was achieved, the cameras were rigidly fixed to the camera stand. For placement of specimen on the impact fixture (figure 1) the entire rigid setup is rolled away from the impact cage, specimen is secured, then the entire setup is rolled back in. The new setup ensures that the camera position, with respect to the fixture and the specimens, remains unchanged, thereby negating the need for re-calibration after each test.

3.1.3. CAI setup

Compression After Impact (CAI) testing followed the ASTM D7137 standard with an adaptation to the load frame in order to match 178 x 178 mm (7” x 7”) panel size [19]. The CAI fixture shown in figure 3 used two flat parallel steel plates for the top clamp and the bottom base for a length of 12.7 mm (0.5”). Two vertical knife-edge supports held the test specimen 12.7 mm from each side edge in the fixture. Overall, the fixture enforces clamped boundary condition in the loading direction, and free boundary condition along the transverse directions. The top and bottom of the test specimen are clamped. The test specimen was loaded using an MTS

Tension/Compression load frame, with a load cell capacity of 500 kN (110 Kip). The MTS recorded load, time, and displacement histories for the experiment. To accurately capture the displacement of the sample in the compression test, 2D DIC was performed on both the front-facing and back-facing surfaces of the test specimen. Two grasshopper cameras were used to image each surface of the test specimen, with impacted surface imaged by the front-facing camera. These cameras were set up so that they were centered and focused on the respective faces of the test specimen. The cameras used an aperture of 11 and a focal length of 25 mm when positioned 120 cm normal to the surface of the test specimen. Vertical displacement was calculated at both the top and bottom regions next to the clamped boundary. The difference between the top and bottom displacements yielded the gauge displacement of the sample.

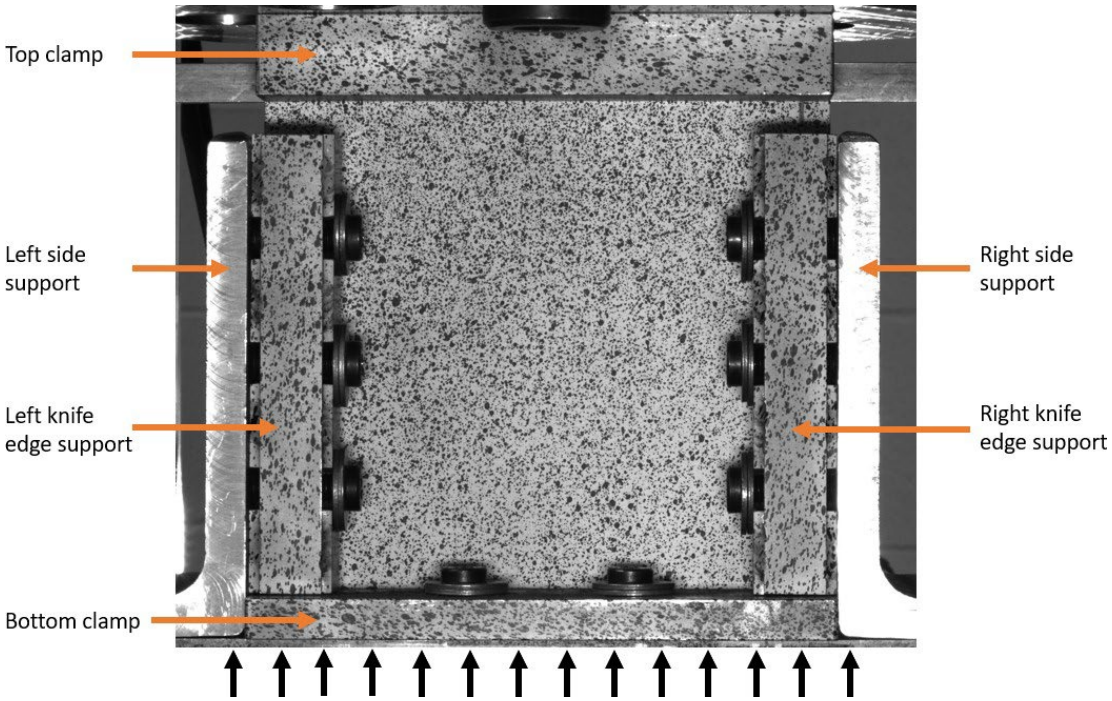

Figure 3 CAI fixture

The fixture was positioned in the load frame such that the test specimen was centered with respect to the machine, to avoid any load eccentricity. Roughly 10 kN of axial pre-load was applied to negate any machine and load frame compliance. The cameras recorded the specimen for the pre- load and measured the strain and displacement of the sample. The 2D DIC measurement ensured that the strains at these locations were equivalent to ensure uniform and non-eccentric loading, in compliance with ASTM standards.

3.2. Experimental protocol

A set experimental protocol was followed for each specimen tested. First, impact test was conducted, followed by post-impact measurements, and then compression after impact test was conducted. Each step of the experimental protocol and outputs generated are described below.

3.2.1. Impact testing

3.2.1.1. Impact procedure

The impact energy and impact point offset were adjusted based on specimen thickness and test schedule. Drop tower optical sensor placement was adjusted based on specimen height in order for the Data Acquisition System (DAS) and the high-speed cameras to synchronously trigger, prior to the impact event. A high voltage lamp was used for the experiment to provide sufficient illumination for the impact chamber and specimen. After each test, the camera system was rolled along the flow rails, away from the Instron impact chamber. The test specimen was taken out of the steel impact fixture. The next sample was then placed onto the impact fixture and secured on the roller supports. The entire set was then rolled back to the locked test ready position. Impact load-time history was recorded by the Instron CEAST software. Entire test sequence images were recorded using high-speed cameras and were analyzed using ARAMIS DIC software.

3.2.1.2. Drop tower measurements

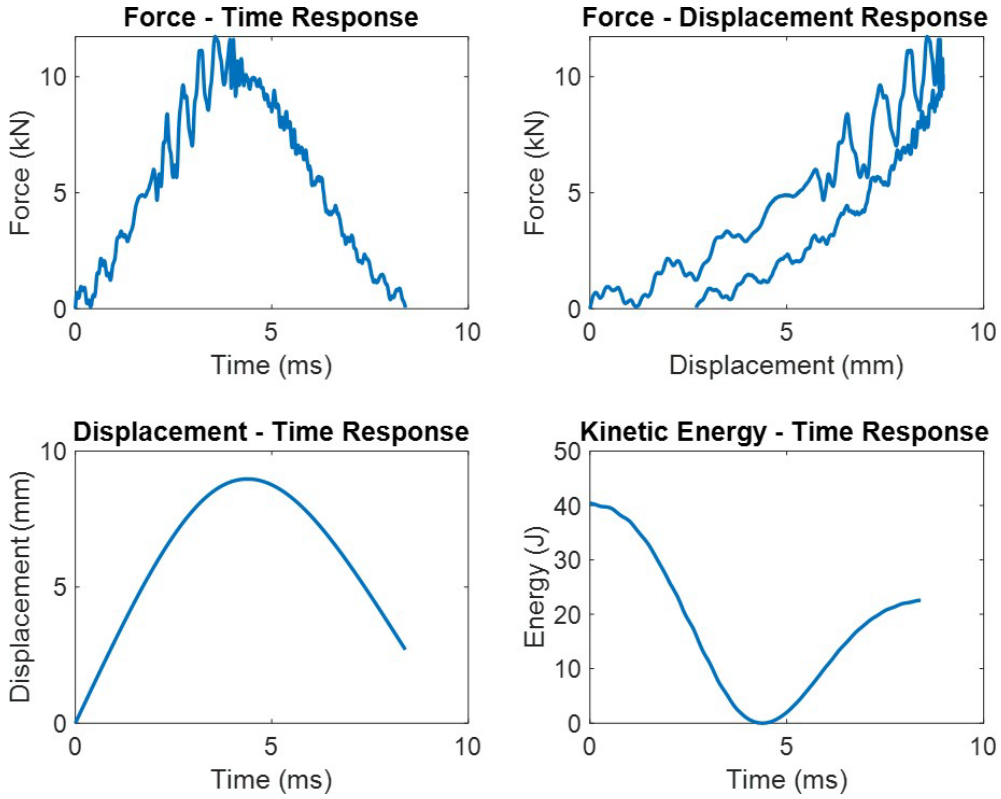

Figure 4 Instron data outputs

Instron drop tower records the force, impactor displacement, impactor kinetic energy, and time of the impact event. Data is recorded at a frequency of 1000 KHz. Figure 4 shows the typical force-time, force-displacement, displacement-time, and kinetic energy-time response obtained from drop tower software. It is observed that force-time response curve has a general shape of a Gaussian pulse with additional frequencies related to events during the impact, which is explained further in later sections of this document. The force-displacement history provides the residual displacement, where the measured load is zero during impactor rebound. The residual displacement

points to fact that there is permanent damage in the composite. The displacement-time response of the impactor is a smooth curve, as it is the measure of impactor motion. The kinetic energy-time response shows the kinetic energy of the impactor over the course of the impact event.

3.2.1.3. 3D DIC measurements

Images from the impact events are post processed using Aramis 3D DIC software, which calculates the global displacements and strains on the bottom surface of the composite.

Figure 5 shows typical images taken from the high-speed cameras with DIC results overlaid on the specimen image. Figure 10a shows the calculated out of plane displacement field experienced by the test specimen. A von Mises strain concentration is observed in figure 10b at the center where the matrix split initiates. Von Mises strain is only used to identify the time and location of initiation of matrix split.

From the DIC data, further information of the specimen deformation is obtained. Figure 6a shows the maximum displacement vs time at the center of the bottom surface of the composite. Colored markers indicate the displacement at 0.8ms. Figure 6b shows the corresponding cross section of the evolving displacement profile. The displacement profile while initially smooth, subsequently shows localized deformation beginning to take shape at the center of the bottom surface, indicating localized damage.

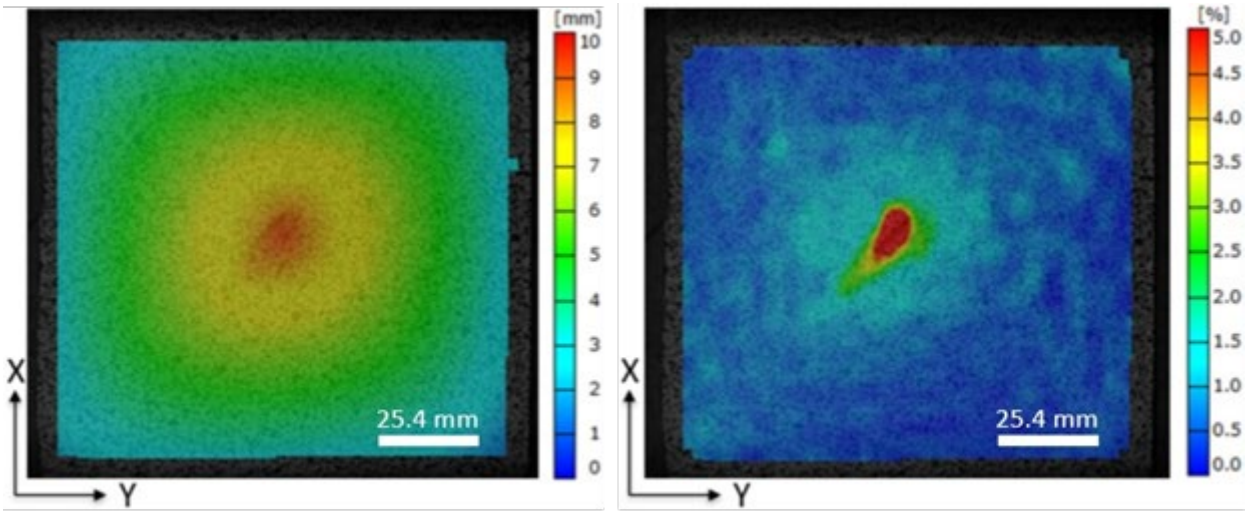

(a) Out-of-plane (Z) displacement field (b) Von Mises strain field

Figure 5 3D DIC measurements

3.2.1.4. Post impact measurements

The post impact measurements included dent depth on the top impacted side of the panel, bottom surface matrix split length, images of the samples, and UT scan.

An initial measurement for the dent depth was recorded immediately after the impact. A second dent measurement was performed at least two weeks after the impact experiment. This was done using a dial gauge which measured the maximum dent depth to the nearest thousandth of an inch.

Two measurements were taken to observe if a change in the dent depth occurred well after the impact.

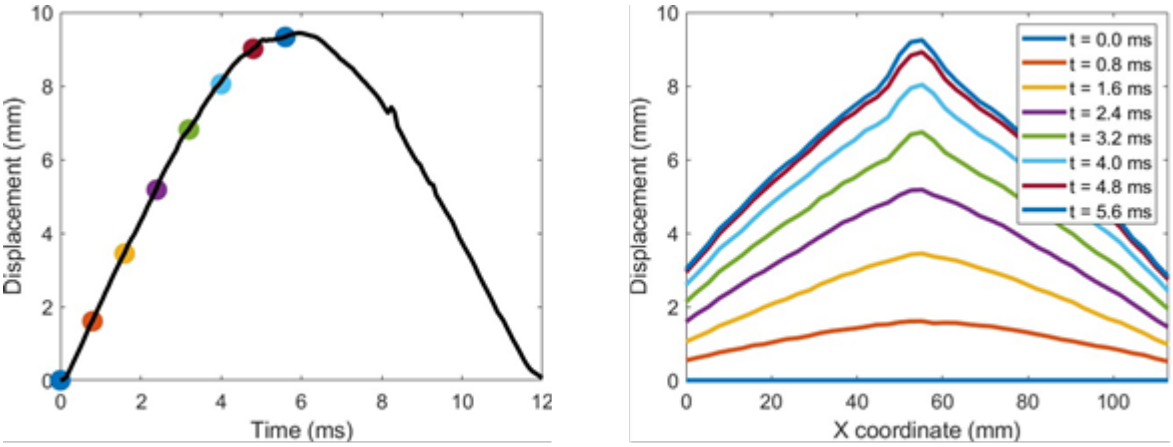

(a) DIC maximum back surface displacement vs. time

(b) Out-of-plane (Z) displacement profile

Figure 6 DIC out-of-plane displacement

Next, the bottom surface of the panel was inspected for matrix splitting. For specimens with matrix splitting, the length of the maximum crack was measured. In cases where top surface (impact side) fiber breakage was observed, the width of failure was recorded. Images of both top and bottom surfaces were taken camera 0.5m above the sample.

All samples were inspected using the Dolphicam2 ultrasound scanner. The scan was performed by using a 5 MHz transducer that captured a 32 mm by 32 mm region at a time. These scans were stitched together for samples with delaminations that extend past the area for a single capture. A gel coupling (Eco SuperGel) was used between the transducer and the sample to reduce noise in the signal and gave a clear inspection of the internal damage. Time Of Flight (TOF) signal provided information on the depth of damage within a sample by recording the time required for a signal to pass into the material and reflect off damage back to the transducer. Combining this information with the speed of the signal and the known thickness of the sample the depth of damage was calculated. The UT scan was saved in a H5 file format for additional analysis. It is to be noted that a UT signal is reflected from the topmost delamination detected at given location. The signal cannot provide any information on the delamination below the topmost delamination. Hence, UT scan only provides a top-down view of damage, and not the complete damage pattern.

3.2.2. Compression after impact testing

3.2.2.1. CAI procedure

After impact testing and post-impact measurements, CAI test were conducted. Each specimen was securely clamped within the CAI fixture. The specimen was aligned such that its face is parallel with the front facing edge of the base fixture. Electronic level gauge was used to ensure each component of the CAI test fixture was assembled correctly. The cameras were checked to ensure that the image of the test specimen was perpendicular and in focus. The LED lights were positioned to provide a clear image of the panel. The DIC cameras were triggered using a function generator

to record one image per second prior to starting the MTS. Twenty reference images were taken prior to loading.

Each test was performed with a loading rate of 0.0127 mm (0.0005 inches) per second and run until sample failure. After the test was completed, images were taken of the test specimen in its failed state before releasing the remainder of the MTS load. Data from the MTS and DIC cameras were then exported and the CAI fixture was taken down from the MTS. The fixture was disassembled and the sample was removed and imaged.

3.2.2.2. CAI measurement

The load-displacement response of specimen under CAI testing is obtained by combining load cell data and 2D DIC data. The MTS records data at 100 Hz during the quasi-static experiment. The 2D DIC measures the gauge displacement of each surface of the composite by subtracting the displacement of the top of the sample from the bottom of the sample on each surface. The DIC measurement for gauge displacement is chosen over the MTS measured displacement because the DIC measured displacement gives the true representation of the displacement of the sample and removes error from potential machine or test fixture compliance.

Figure 7 shows a typical load displacement relationship obtained for the samples tested. Classical Lamination Theory (CLT) was used to predict the linear axial response of the specimen and is shown using the dashed red line in the figure, using material properties provided in Appendix B. There is a distinct deviation from the linear response early in the loading history, which indicated Euler buckling of the specimens. The buckling event was confirmed by the strain analysis of front and back surface of the specimen.

The strains shown in figure 8 are global strains recorded at the center of the front and back surfaces on the F16 test specimen. In its pre-buckled state, the strains on both surfaces experience a compressive strain of the same magnitude. When the buckling load is reached, the front and back strain measures deviate, indicating out-of-plane bending. The divergence of the strains was used to identify the point where buckling initiates during the experiment.

From the load time history, and the buckling strain analysis, the buckling and ultimate failure loads were obtained.

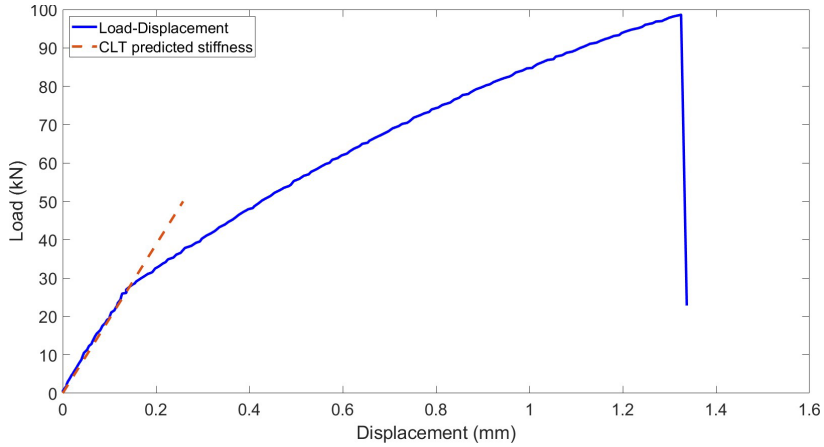

Figure 7 CAI Load Displacement Relationship for thin (top) and thick (bottom) composite

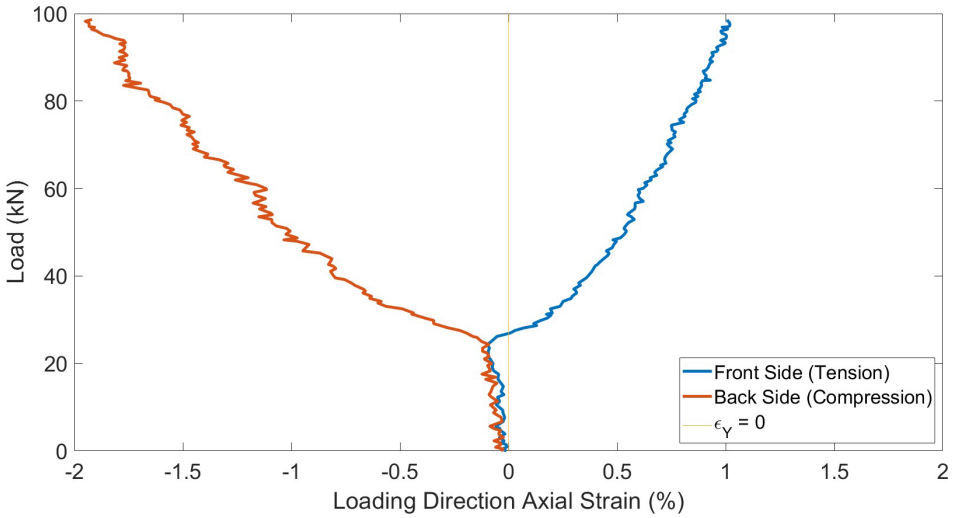

Figure 8 CAI strain measurement

4. RESULTS AND DISCUSSION

4.1. Results: Impact test

4.1.1. Results from force-time and displacement-time response

Figure 9 compares the force-time response of F16 and F24 specimens at 10J, 15J, 25J, and 40J. As is expected with each increase in impact energy, the overall profile shows an increase in peak load, for each both F16 and F24. The complete force-time responses at all tested impact energies are provided in Appendix C. The figure also illustrates the variety in response. With increase in impact energy there is a distinct increase the secondary oscillations within the response. In this section the focus is on general trends gained from the overall impact results.

Figure 9 also compares the force-time response of WL40, WU48 and WL56 specimens at 30J, 40J, 60J, and 80J. As is expected with each increase in impact energy, the overall profile of shows an increase in peak load for each composite. The complete force-time responses at all tested impact

energies are provided in Appendix C. Figure 9 also illustrates the variety in response. With increase in impact energy there is a distinct increase the secondary oscillations within the response.

Figure 10 shows the 40 J impact for each of the five composite layups. As the bending stiffness of the composites increases due to their stacking sequence and overall thickness, the composites experience a stiffer response to the impact, produce a higher reaction force, and a lower maximum displacement experienced by the impactor.

From the force-time and displacement-time response, the maximum force and displacement experienced by the impactor can be obtained. Figure 11 shows the comparison of maximum impactor force and maximum impactor displacement at increasing energy levels for the thick composites. The maximum load increases from 9kN to 22kN in the WL40 composite between 15J to 80J. The WU48 composite increases from 12kN to 24kN between 20J and 100J. The WL56 composite increases from 17kN to 29kN between 30J and 100J. The WL40 composite experiences the most out of plane displacement while the WL56 composite experiences the least out of plane displacement. This is consistent with the fact that compliance of the composite decreases as the number of plies increases.

Figure 12 shows the residual displacement of the impactor obtained from displacement-time history, which indicates the presence of permanent indentation or damage in impacted specimen. Each composite experiences an increase in residual displacement with increasing impact energy. This relationship is fairly linear over the experimental impact energy range. A local increase in the residual displacement is observed in the measurements on either side of the impact energy threshold for delamination initiation.

The kinetic energy lost by the impactor is calculated from the force-time and displacement- time history, with the assumption that energy lost due to friction is negligible. Figure 13b shows the amount of kinetic energy lost from the impactor at each impact energy level. Each configuration shows a linear increase in the kinetic energy loss as impact energy increases. Each composite shows a sharp rise in the kinetic energy loss at the lowest impact energy in which delamination is detected, most notably between 30J and 40J for the WU48 and WL56 specimens. The sudden increase in impactor energy loss is an indicator of sudden increase in damage within the composite.

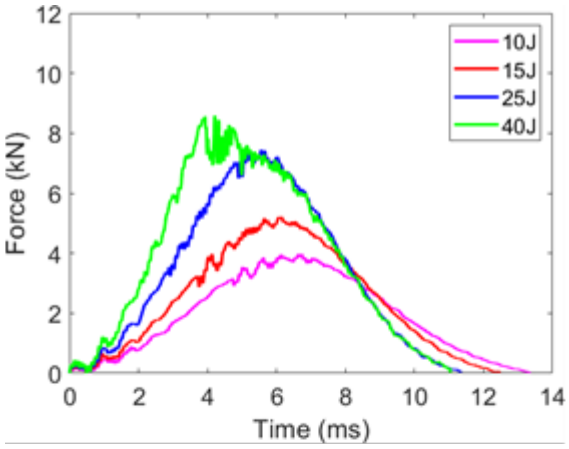

(a) F16 force - time response

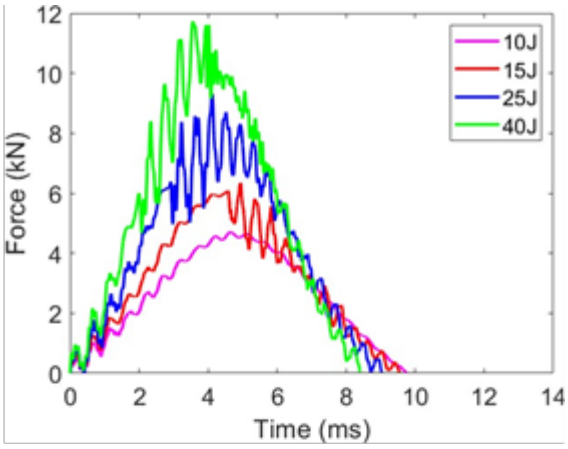

(b) F24 force - time response

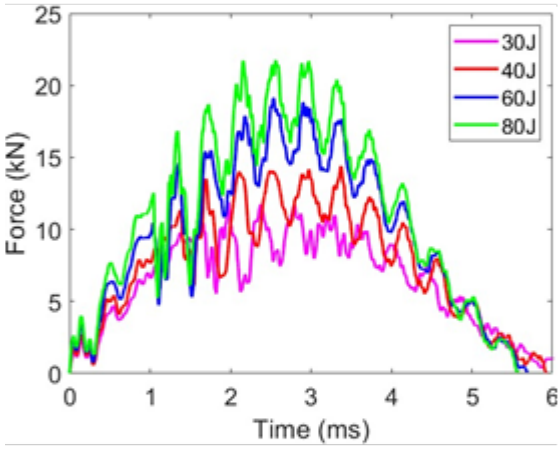

(c) WL40 force - time response

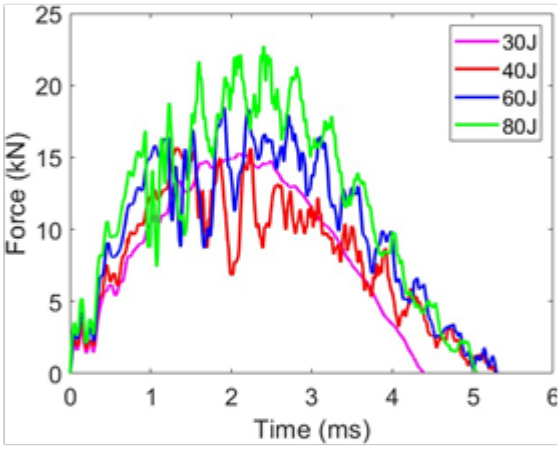

(d) WU48 force - time response

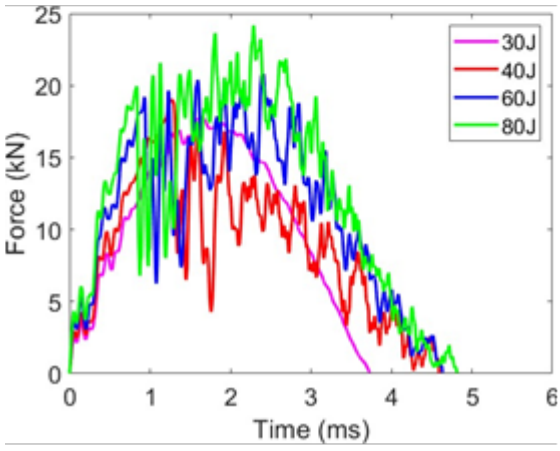

(e) WL56 force - time response

Figure 9 Impact response

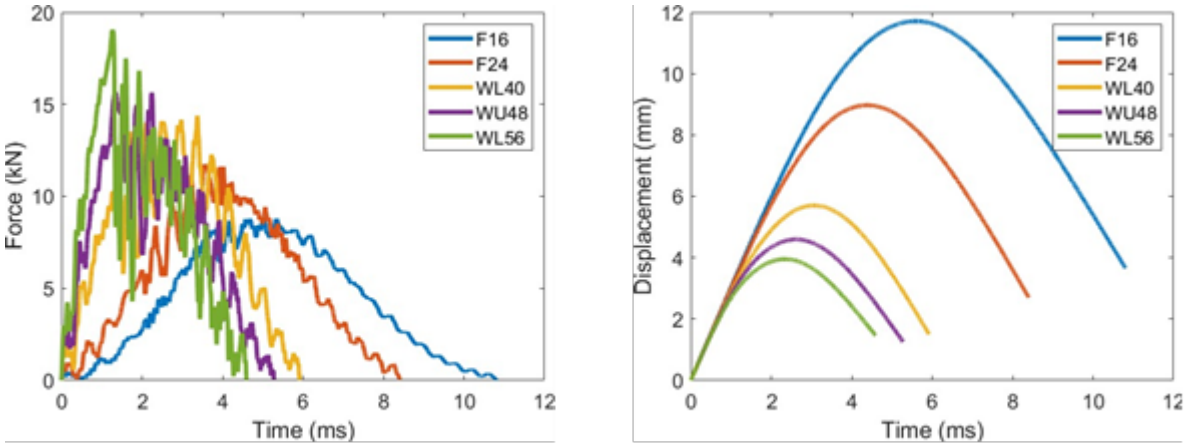

(a) Force vs. Time response (b) Displacement vs. Time response

Figure 10 Impact response comparison at 40J

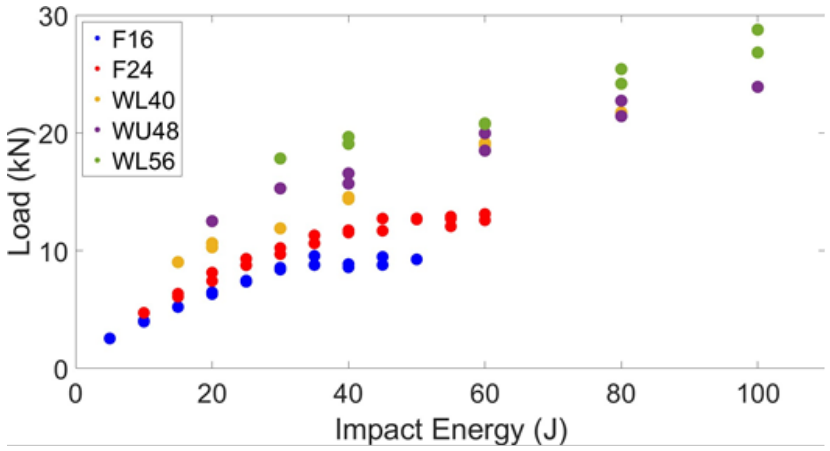

(a) Impactor Maximum Load

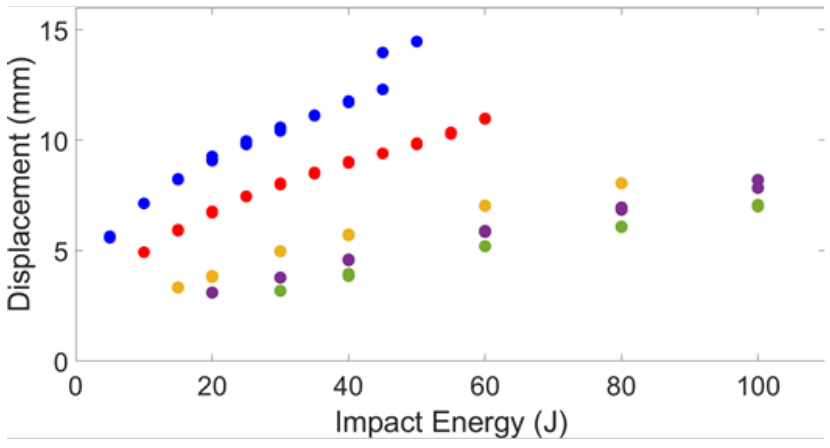

(b) Impactor Maximum Displacement

Figure 11 Impactor maximum load and displacement

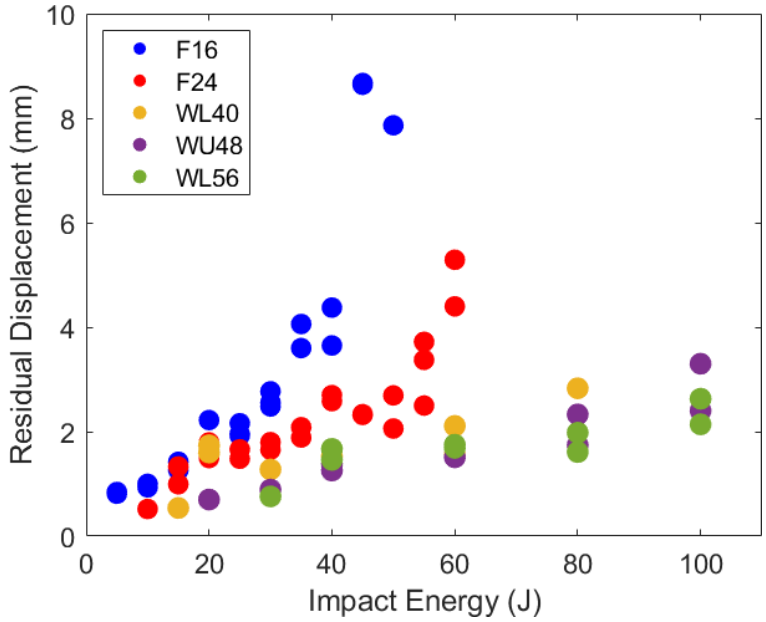

Figure 12 Residual displacement of impactor

4.1.2. Results from 3D DIC analysis

Measurements from the DIC analysis yields the relationship between maximum bottom surface displacement and impact energy, as shown in figure 14. The trend in result is consistent with the impactor displacement measurements show in figure 11. The DIC analysis also provided the bottom surface strain measure during the impact event. For each specimen global strains, and the frame at which splitting initiates was recorded. Figure 16 shows an image of a back surface matrix split from the view of the high-speed camera during the impact experiment. The time at which back surface splitting initiates is identified by inspecting each image frame by frame until a split in the matrix is observed. The frame where splitting initiates is converted into an equivalent time points for the impact duration. The red box shows the region where the observed split at a time point well after the split has initiated.

The global strains were then converted into local strains based on the orientation of the bottom ply fiber direction. Figure 15 shows an example of local strains developed on the bottom ply with fibers oriented at 45◦. The black marker indicated the point, during the impact event, when back splitting is first observed. As the strain in the transverse strain (ε22) is larger than the shear strain

(ε12), the failure mode is understood to be matrix mode-I dominated. Hence, the result provides the failure strain required to cause matrix splitting during an impact event.

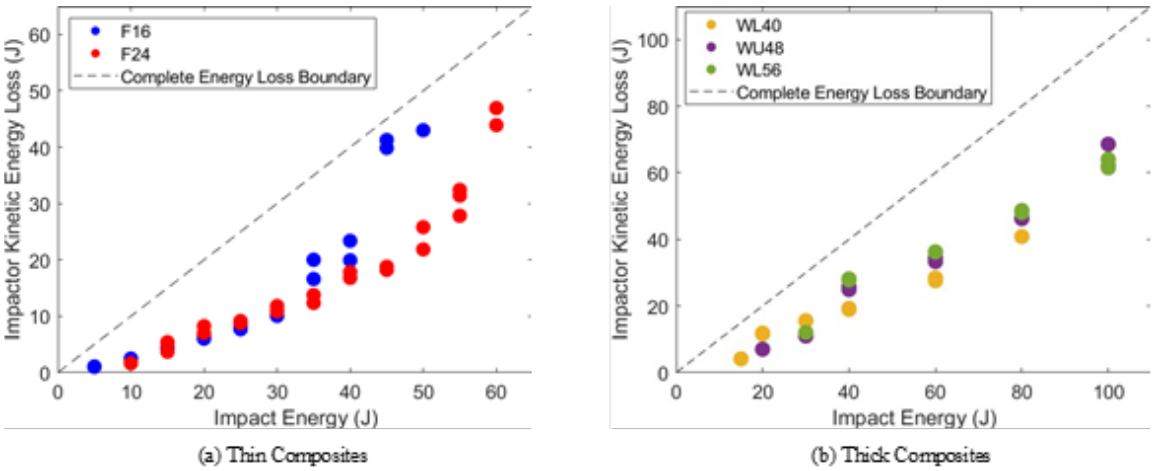

Figure 13 Impactor Energy Loss vs. Impact Energy

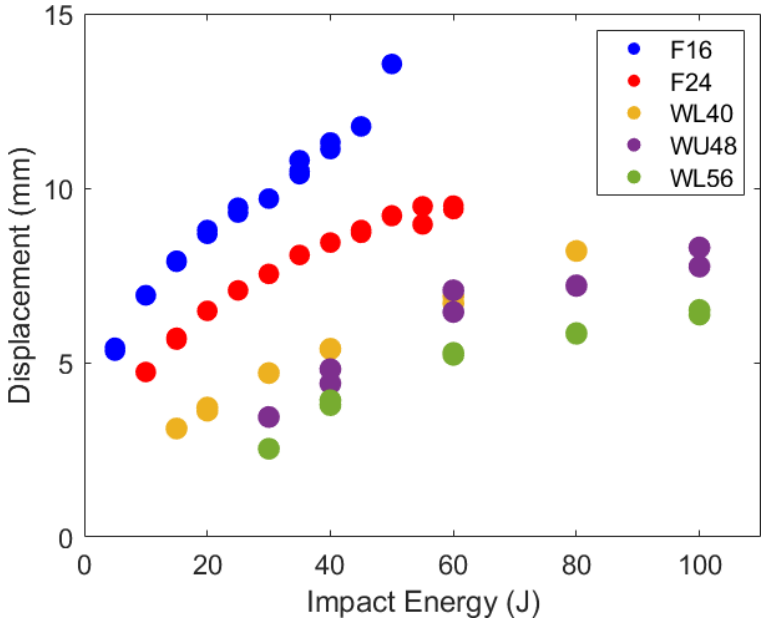

Figure 14 Bottom Surface Maximum Displacement

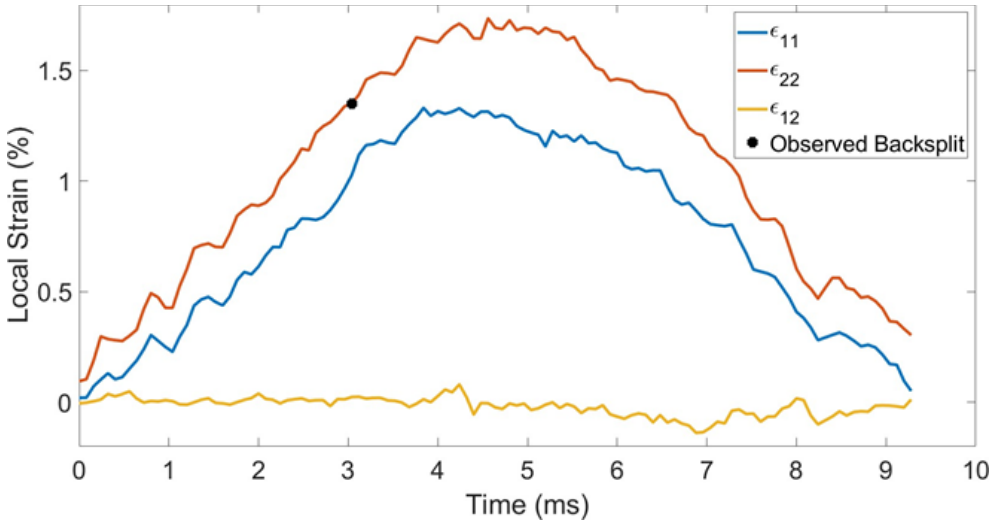

Figure 15 Local Strain recording from 3D DIC

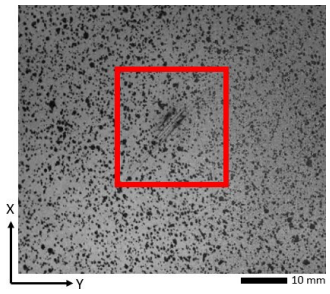

Figure 16 Visible back surface splitting initiation

4.2. Results: Post Impact measurements

4.2.1. Impacted Surface Dent Depth

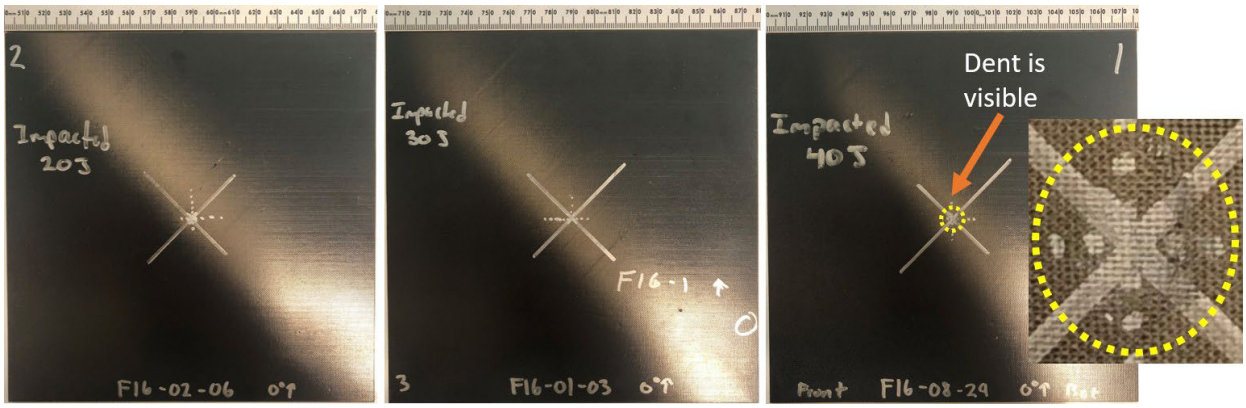

Figure 17 Observed Impact surface of F16 at 20J, 30J, 40J

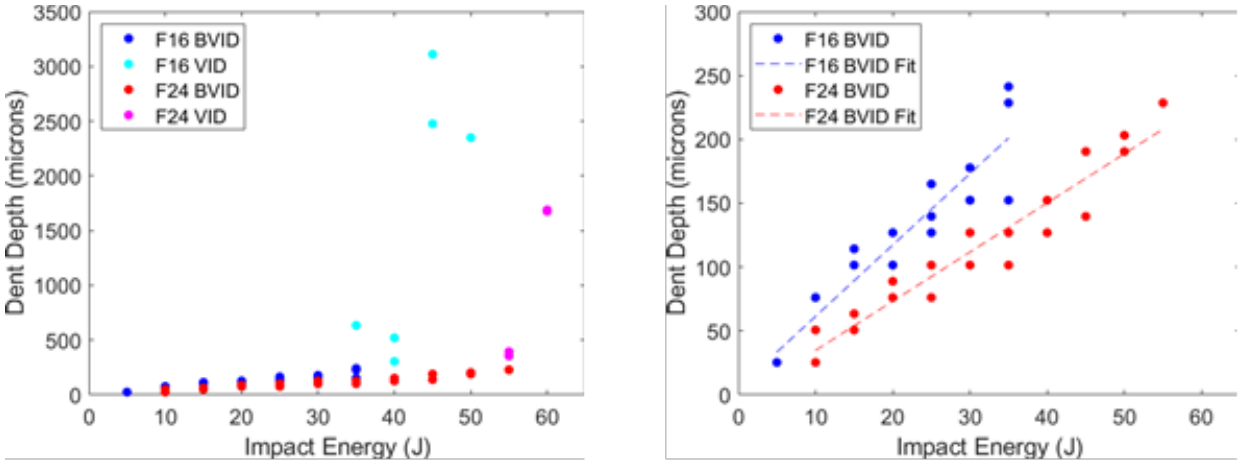

(a) Top surface dent depth measurement (b) BVID top surface dent depth measurement

Figure 18 Impact dent measurement.

Figure 17 shows an example of kind of damage seen on the impacted surface of F16 composites at 20J, 30J and 40J. At 20J and 30J impacts there is no obvious or detectable sign of impact damage on the sample surface. On the other hand, at 40J an indentation is visible on the top surface of the sample.

Utilizing the typical commercial aircraft BVID dent depth criteria of 300µm, the results can be categorized as Visible Impact Damage (VID) or BVID. Figure 18a plots the relationship between the measured dent depth and the associated impact energy, categorized as VID or BVID. The experiments considered to be below the BVID limit show a linear relationship between dent depth and impact energy in figure 18b. The transition from BVID to VID occurs at 35J in the F16 composite. This same transition occurs at 55J in the F24 composite. In the VID range, the dent is easily seen on visual inspection. Also, at these high energies, top surface fiber compression failure is present, allowing the impactor to partially pass into the composite, generating a larger dent.

Figure 19 plots the dent depth as a function of the impact energy for each specimen. An in- crease in the dent depth correlates with the presence of delamination for each composite. For each thick composite and for every energy level tested, the impacted surface dent depth was small enough such that all samples were considered to have BVID. In the instances where no delamination is present, the dent depth is significantly lower. This behavior is very different than what was observed with the thinner 16 and 24 ply composites. The thin composites had a clear BVID transition energy, in which a threshold impact energy separated BVID and VID. This indication of failure is not observed in the 40, 48 and 56 ply composites.

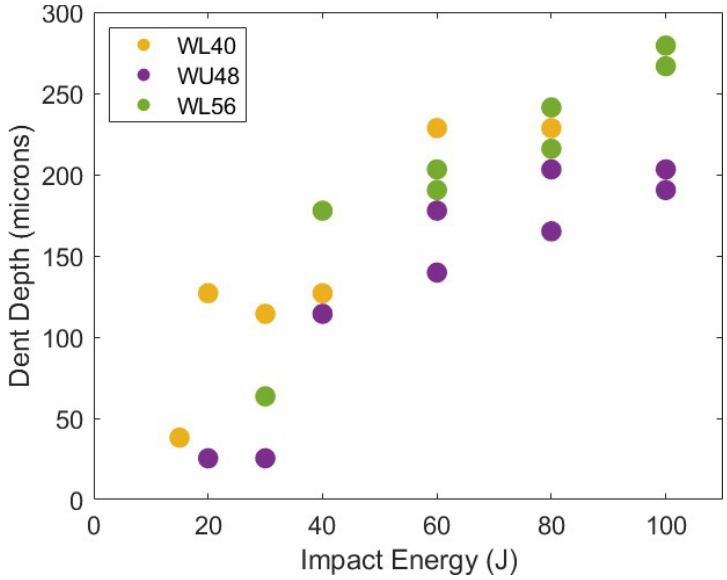

Figure 19 Dent Depth vs. Impact Energy

4.2.2. Bottom surface matrix splitting

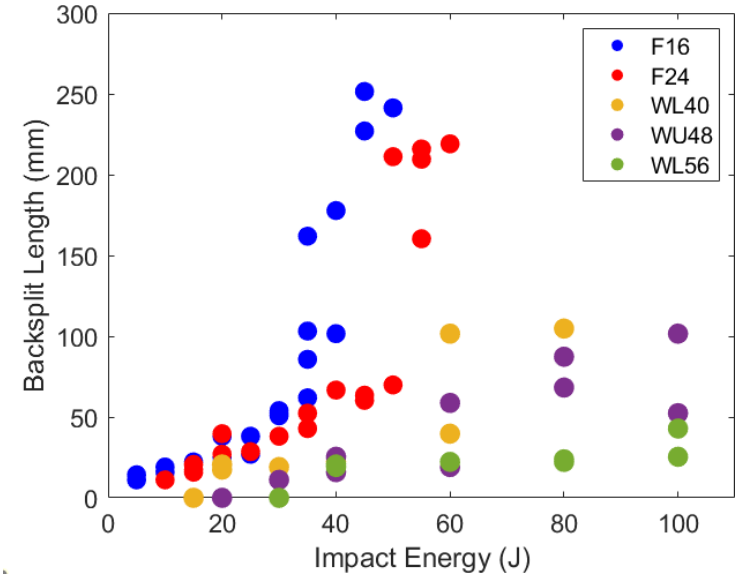

Figure 20 Bottom Surface Matrix Split Length vs. Impact Energy

The next measurement is the bottom surface matrix split length. Not all impacted specimens developed a matrix split. A detected bottom surface matrix split was only present in the samples which also experienced delamination. Figure 20 shows the measurements of the back surface split length. The matrix splitting always initiates at the center of the panel and propagates along the bottom ply fiber direction. The maximum split length possible is 251 mm (9.9 inches), the diagonal length of the panel. The propagation of the matrix split occurs quickly and attributes to the range of data values for this measurement. The WL56 sample consistently experienced the shortest

matrix split lengths. It is important to note that the back split length in the F16 sample experiences a significant jump starting at 35 J, the same energy where the top surface of the panel transitions from BVID to VID. There is also an apparent jump in the back split length for the F24 sample at 55J, where its BVID limit is observed. Below the BVID limit, the relationship between matrix split length and the impact energy is linear.

4.2.3. Ultrasound scan

The third post-impact measurement is the ultrasound scan of the composite. Using the Dolphicam2, a time-of-flight (TOF) scan can be performed on the impacted surface of the sample that provides a top-down view of delamination and internal damage within the composite. The time-of-flight information is combined with the speed that the signal travels through the material to calculate the depth at which the signal reflects, which indicates an associated depth within the composite where the delamination is located.

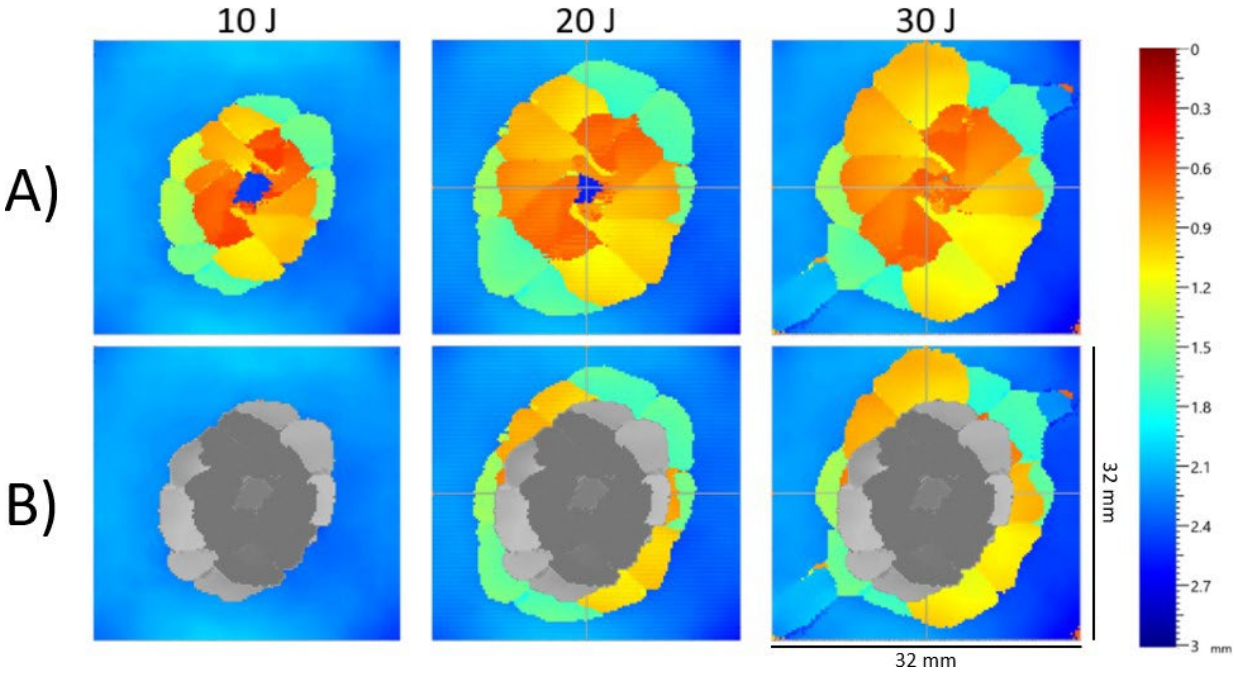

Figure 21 Growth of Delamination Area with Increasing Impact Energy

Using UT scan a clear image of delamination pattern and depth is obtained. Figure 21 and figure 22 show the delamination pattern in thin and thick composites. The scan also highlights clear patterns of damage in the sample. A petal shape pattern or a spiraling fan shape through the thickness of the impacted sample. As an example, figure 21-row A, shows the delamination extent, depth and pattern in a F16 composite impacted at 10J, 20J, and 30J. In row B, the F16 10J impact event is taken in grayscale and superimposed onto the other impact damage patterns, which highlights the uneven increase in delamination area, indicating preferential interfaces for delamination growth with increase in impact energy.

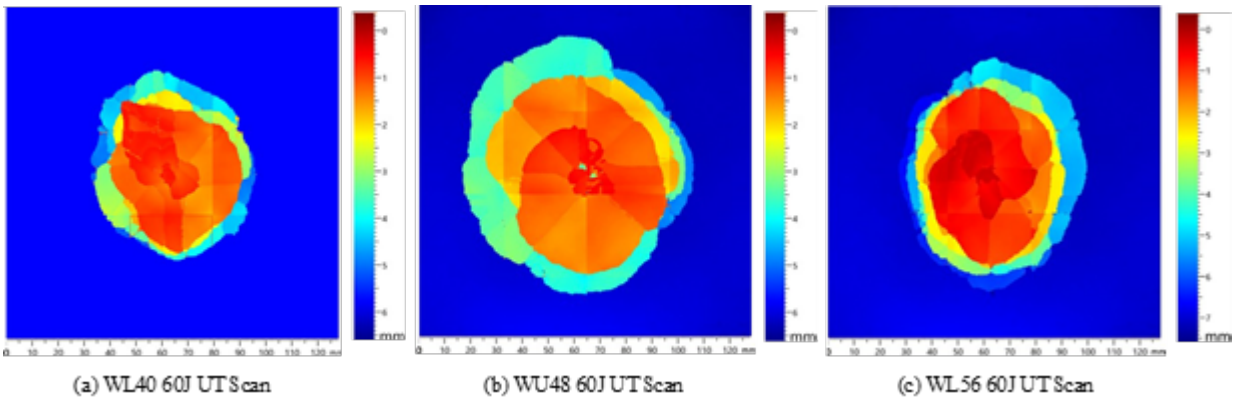

Figure 22 Ultrasound Images of Impacted Composites

From the UT scan images, the overall area of delamination is calculated based on depth value of each pixel in the image. Pixels with depth value less than the thickness of the laminate, indicates the presences of delamination. Hence, by calculating the area covered by such pixels, the total top-down area is calculated. Figure 23 and figure 24 shows the increase of the delamination area as the impact energy increases. The F16 composite experiences delamination at impacts above 5J, the F24 composite did not delaminate in tests at 10J of impact energy and did not delaminate in one of the three impacts at 15J. Therefore, these energies define the impact energy lower bound below which delamination will not occur. Beyond this delamination initiation threshold, the area increased linearly with tested impact energy.

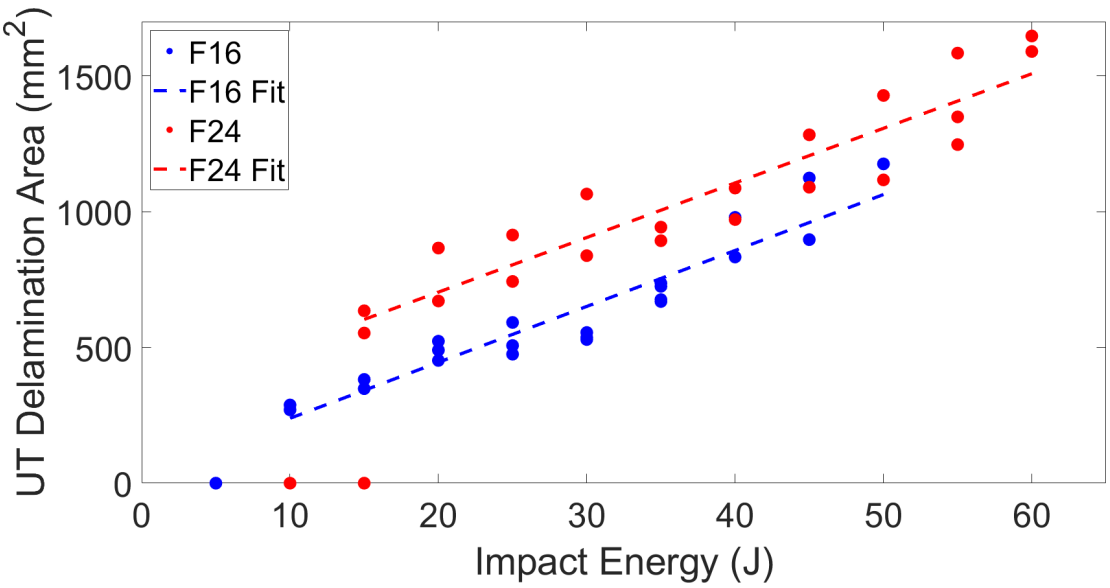

Figure 23 UT Delamination Area Measurement

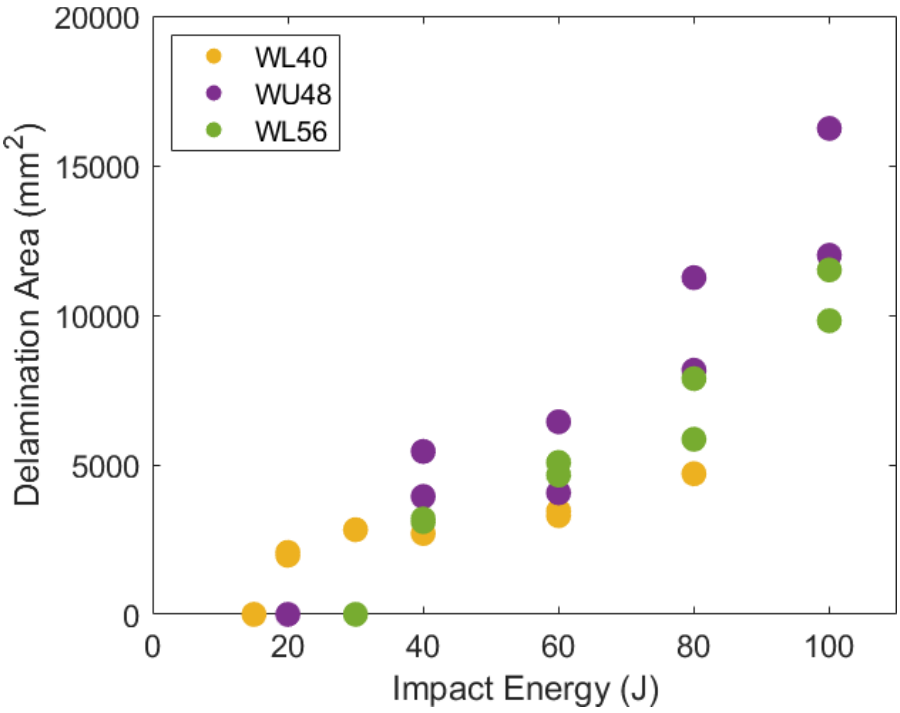

Figure 24: UT Delamination Area vs. Impact Energy

4.3. Results: CAI test

Pristine, un-impacted, specimens were CAI tested first to establish CAI baseline. All impacted specimens were then tested until failure. Figure 29 plots the load vs. displacement response for the WL56 composite. This composite was loaded it its primary 90 degree orientation. Figures 25 and 26 show the load-displacement response for F16 and F24 specimens respectively. Both laminate configurations buckle before reaching their ultimate load regardless of the extent of damage to the test specimen. The buckling load is identified by a noticeable change in slope of the load-displacement response. An ultimate load knockdown is also observed in each of the composites. The F16 composites have a very similar loading path from the pristine case up to between the pristine case up to 35 J fail at a similar load and displacement, while an ultimate load knockdown is observed in the panels with a higher extent of damage.

The images in figure 30 show how CAI test specimens fail at varying impact energies. Images 30a and 30b compare the CAI failure for the F16 specimen which were impacted at 10J and 35J. Images 30c and 30d compare the CAI failure for the F24 specimen which were impacted at 15J and 45J. The blue box in each image represents the region on the bottom (non-impacted) surface of the composite where matrix splitting occurred. This region is much smaller at lower impact energies. The delaminations in the test specimens are located within the extent of the matrix splitting (the blue box). The red box in each image represents the region where failure due to the CAI experiment is observed. At low energies, the CAI failure region is located near the top of the knife edge supports, and away from the location where internal delaminations are present. However, at higher energies the CAI failure region passed directly through the impact induced delamination.

Figure 31 plots the buckling load and ultimate load against the prescribed impact energy for each test specimen. The vertical lines represent the BVID limit for each composite. For both composites, there is little change in the buckling load regardless of the impact energy. The ultimate loads in the CAI experiment for both composites decrease at higher impact energies.

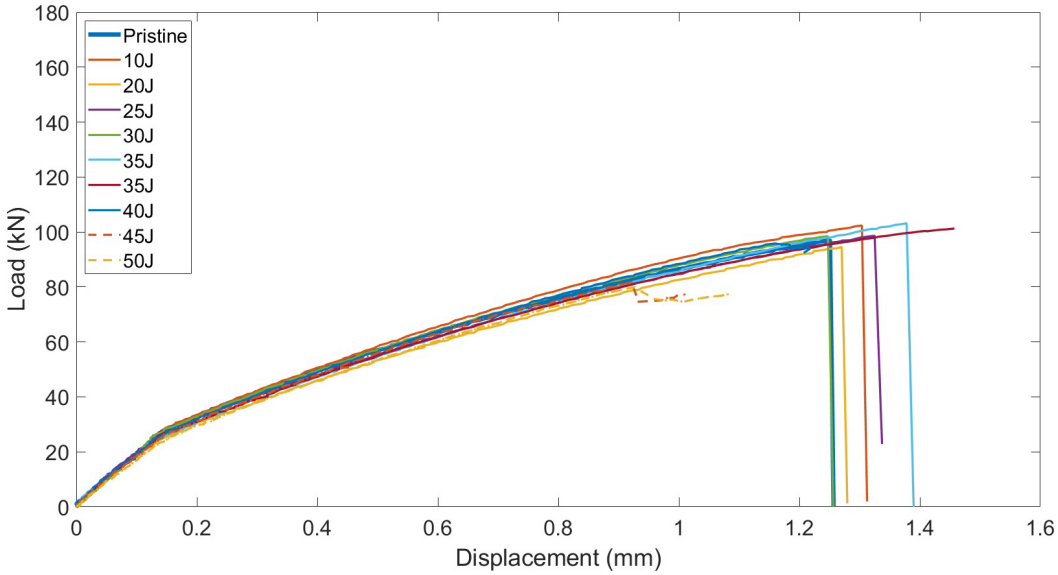

Figure 25: F16 CAI load - displacement relationship

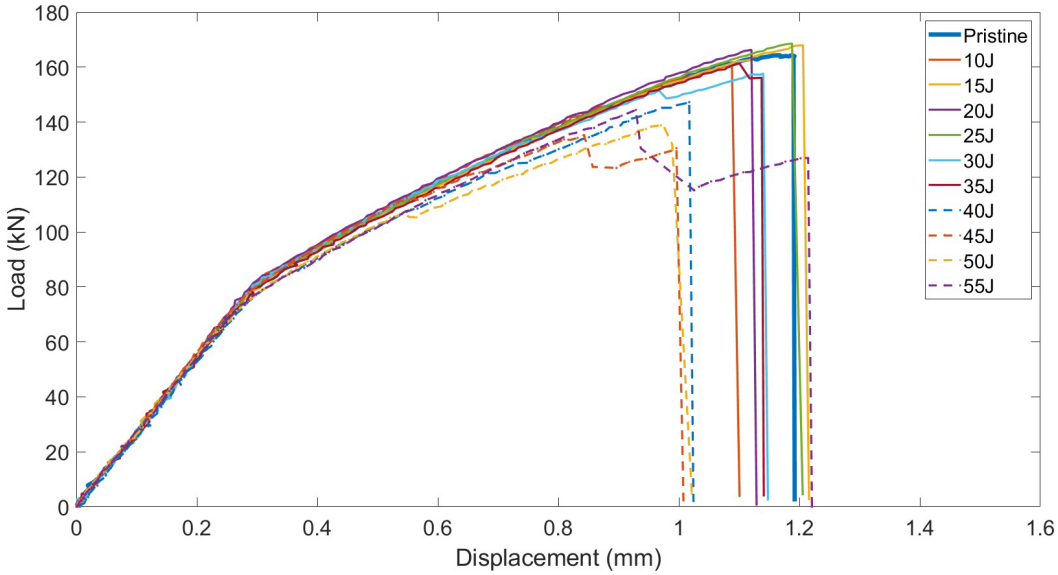

Figure 26: F24 CAI load - displacement relationship

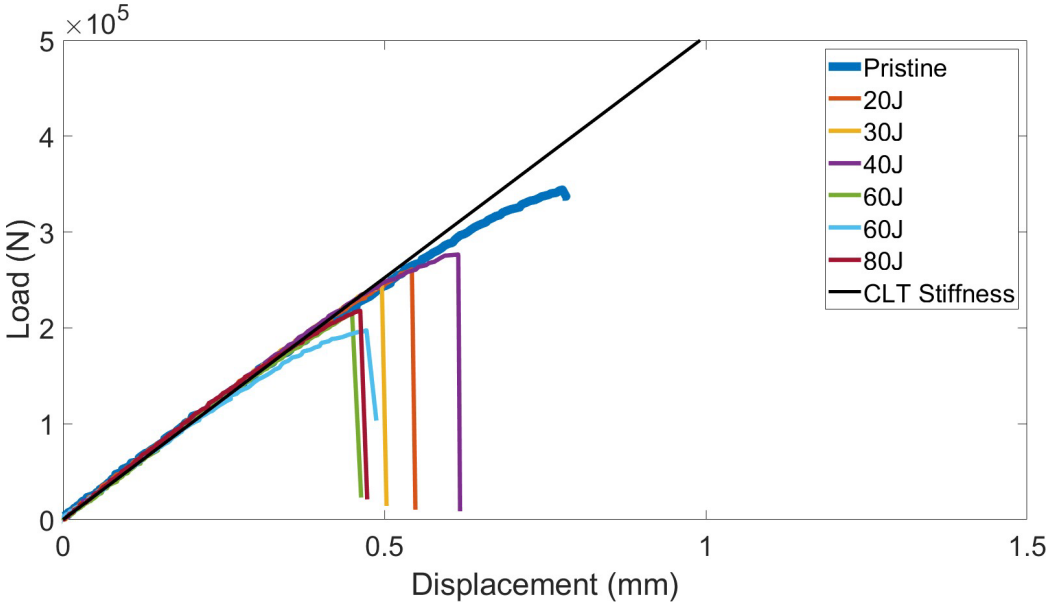

Figure 27: WL40 CAI Load vs. Displacement

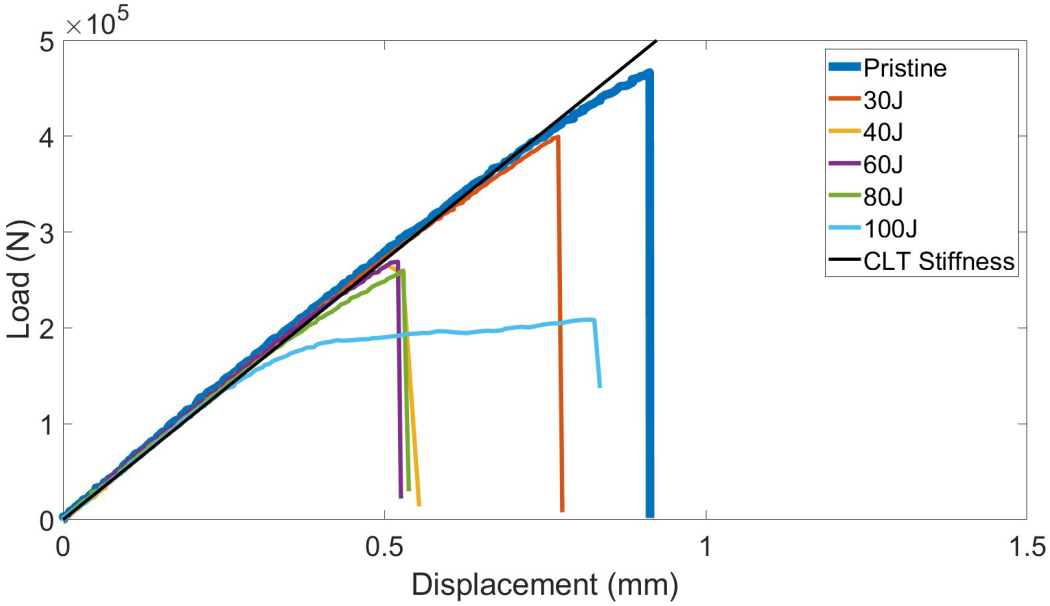

Figure 28: WU48 CAI Load vs. Displacement

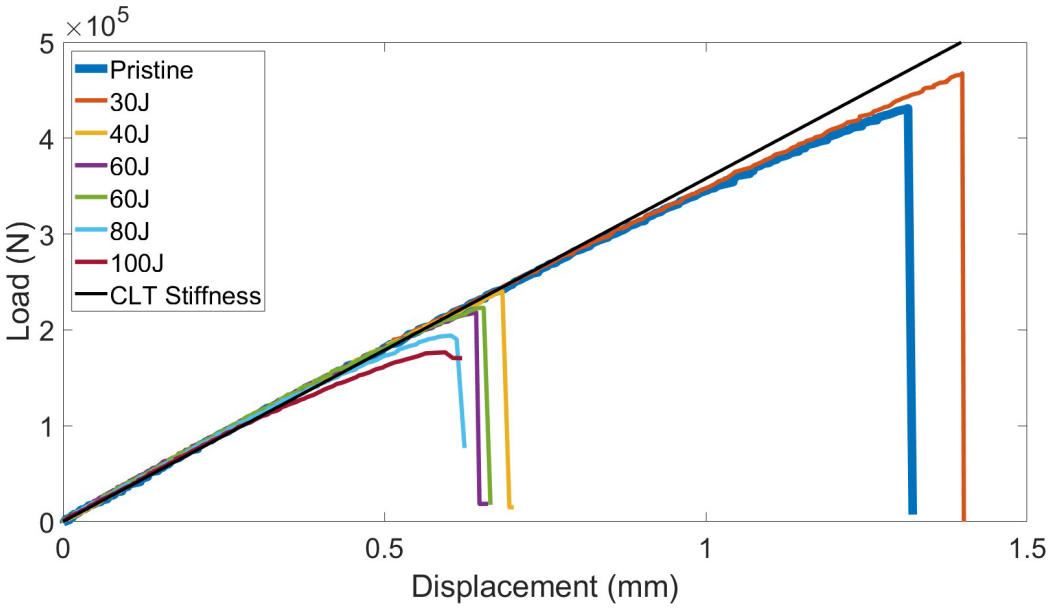

Figure 29: WL56 CAI Load vs. Displacement

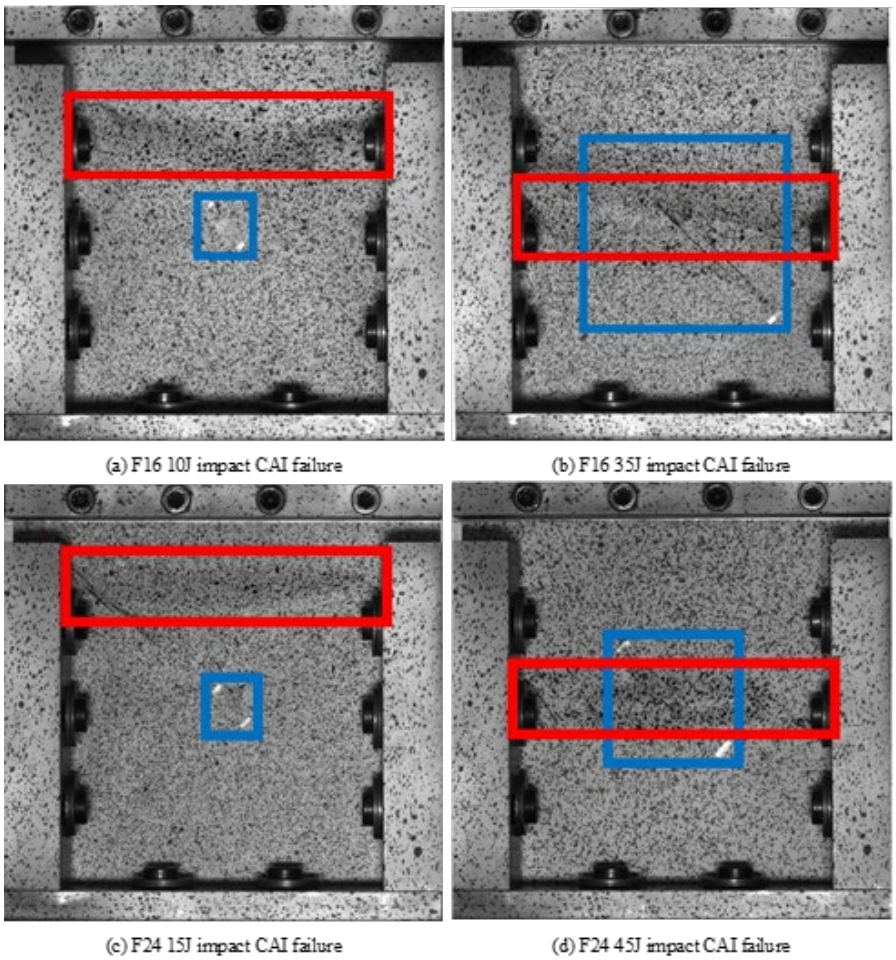

Figure 30: Qualitative CAI failure images

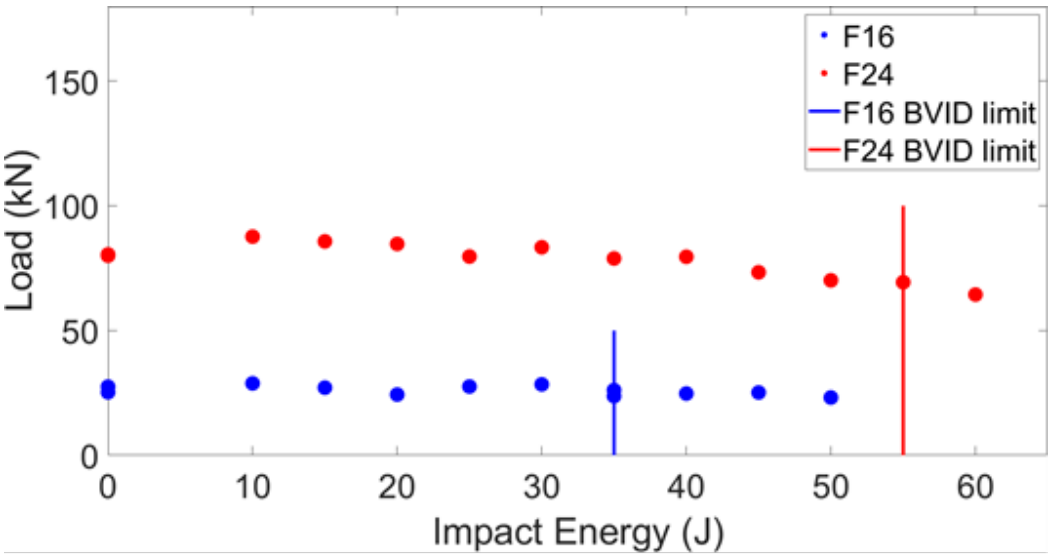

(a) Buckling load vs. impact energy

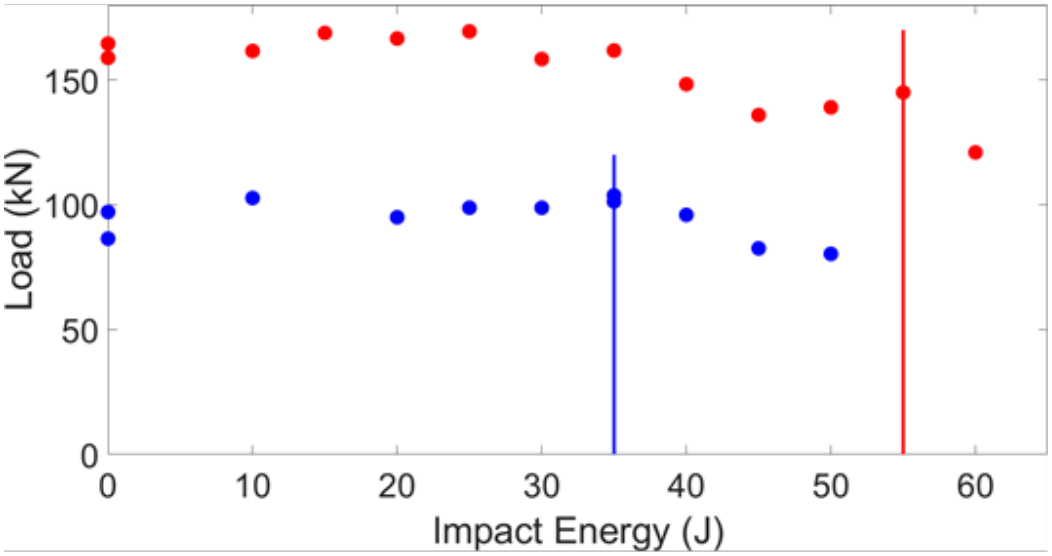

(b) Ultimate load vs. impact energy

Figure 31: Buckling and ultimate loads with respect to the prescribed impact energy

4.4. Analysis

4.4.1. Impact analysis – Thin composites

During the course of testing, three different impact response were observed. For both specimen thicknesses, at lower energies, the force-time history showed a typical primary Gaussian pulse response, with low frequency oscillations diminishing with time, as shown in 32a. Subsequent UT scans indicated that specimens with such force-time histories do not show any delamination,

however, back surface splitting can be observed. As the impact energy was increased, the force-time response initially showed low-frequency behavior, but subsequently, a secondary high amplitude oscillation is recorded, as shown in 32b. Upon UT inspection, these specimens showed delamination and back surface matrix splitting. It can be inferred that he secondary high amplitude oscillation is caused by the sudden energy release due to delamination initiation. Further increase in impact energy showed a tertiary high frequency oscillation in the force-time response, 32c. At these energies, the samples showed visible fiber breakage on the impact surface (top sur- face). Therefore, such tertiary response in force-time history can be attributed to fiber breakage on the impacted surface. The time and load corresponding to the secondary and tertiary events is recorded.

Figure 33 shows that the impactor load at the point of the first significant load drop is different for both the F16 and F24 layups. The F16 samples have a mean load of 3.27 kN, while the F24 samples record a mean load of 6.03 kN. The impactor displacement is also recorded at this point. The displacement value is similar for the composites as the load drops occur at a mean value of 6.38 mm in the F16 samples and a mean value of 5.87 mm in the F24 samples.

The results from this study allow for the order of critical failure events to be identified for the two laminates. The first failure event observed is the bottom surface matrix splitting.

Figure 34 shows the force vs time response for the three impact experiments at 15 J on the F24 composite. Sample F24-02-05 and F24-04-13 each experienced a significant drop in the force recording while sample F24-03-12 (in black) did not. Each of these experiments had observed bottom surface splitting which suggests that the load drop is not caused by matrix splitting.

The corresponding ultrasound scans for these impacts in Figure 35 show that the experiments with the significant load drops have delamination, while the test with no load drop did not have delamination. The three impact experiments at 15 J allow for an inference on the initiation of delamination based on the force vs. time response. It is important to note that even though the three samples shown in Figures 34 and 35 are of the same stacking sequence and impact energy, they produce different results. This variation in the results could arise from minor inaccuracies during the manufacturing process (the force-time response experiences its load drop within a very small margin of its peak load). Minor defects that are not detectable by the UT scan may also influence the delamination growth. The delamination area is calculated by summing the number of nodes that record delamination and multiplying the number of nodes by the tributary area.

The matrix split initiation is easily visible from the images captured in the high-speed camera. The peak displacement is determined from the displacement vs. time relationship from the Instron recording. The delamination initiation is not directly measurable but is inferred using the information provided in the three F24 impacts at 15 J. Combining this information produces a clear progression of failure events during the impact event for these composites.

Figure 36 illustrates the time at which each failure event is initiated during the impact experiment. The magenta markers represent the time points at which back splitting is observed by the high-speed cameras. There is no clear effect on the force time response upon the initiation of this damage initiation event. This is because back surface matrix splitting is a progressive event and the split continues to propagate over the course of the impact. The energy released in this damage is spread out from the point of initiation until the peak load deformation is reached. The blue markers represent the time of the first significant load drop in the force response.

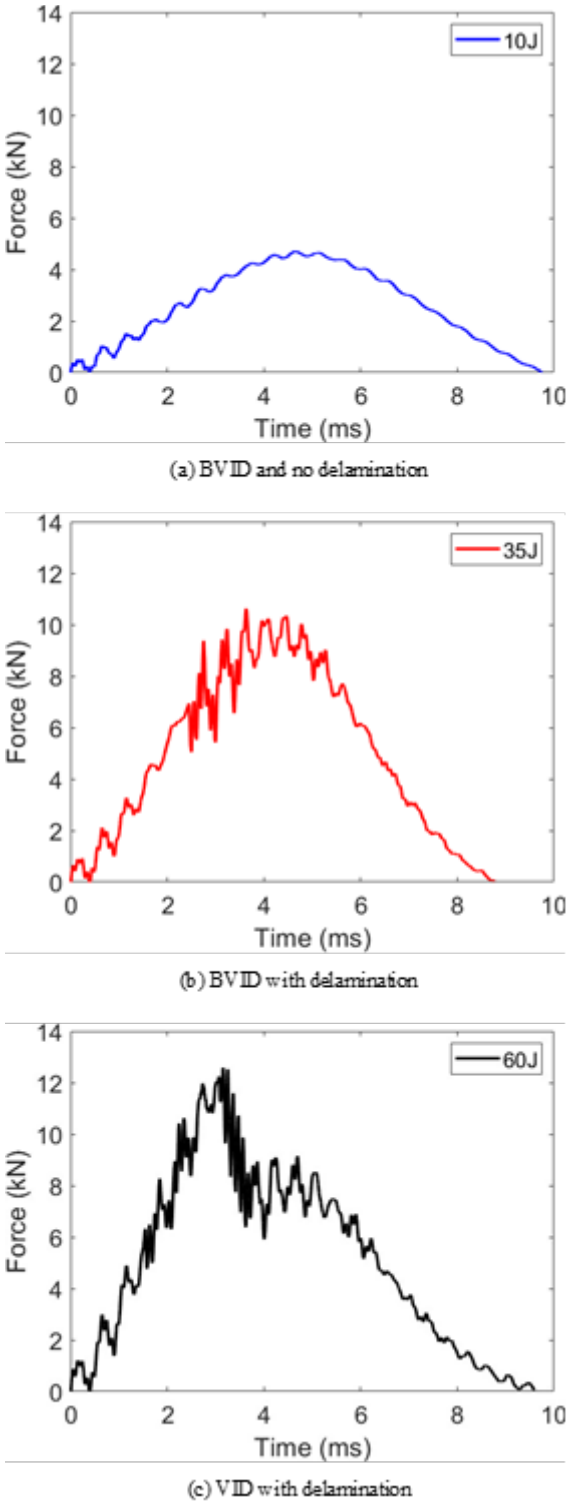

Figure 32: Impact response at various energies on the F24 composite

This is inferred to represent the initiation of delamination. The black markers represent the time of the second significant load drop in the force response of the impact. This is inferred to represent the initiation of visible impact surface damage, in which energy is released during fiber and matrix

failure. The green markers represent the time until peak displacement in reached during the impact event. The minimum time to peak displacement is reached at the BVID limit of each composite. The time to peak displacement decreases as the impact energy is raised and is yet below the BVID. Once top surface failure becomes visible, the impact event is slowed down and the time to peak displacement increases after the BVID limit impact energy.

Figure 36 shows that in the F16 composite, the data between matrix splitting and the first significant load drop do not intersect. These events in the F24 composite occur closer together and start to intersect at higher energies which suggests that the order of failure events may be different based on energy of the impact. This trend may also be different for composites of different stacking sequences or thicknesses.

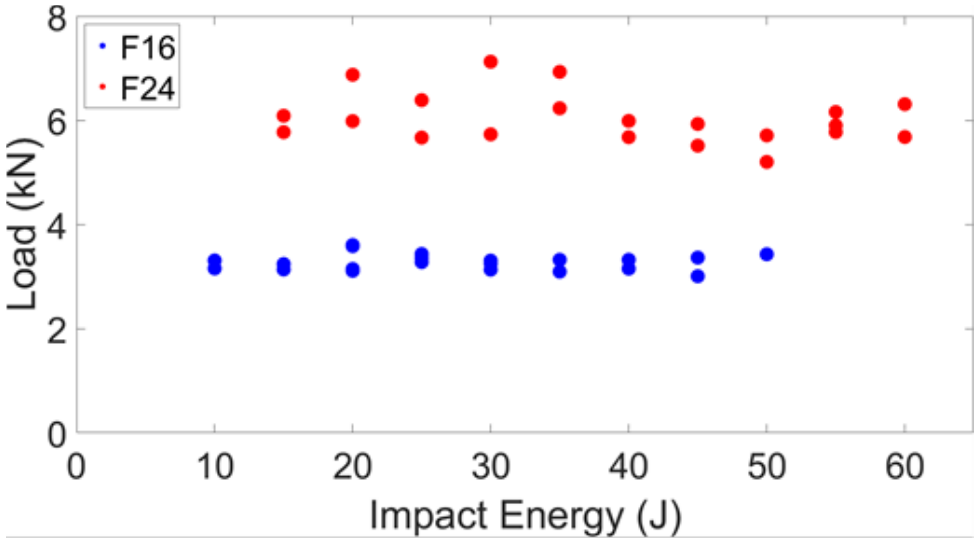

(a) Impactor force at first load drop

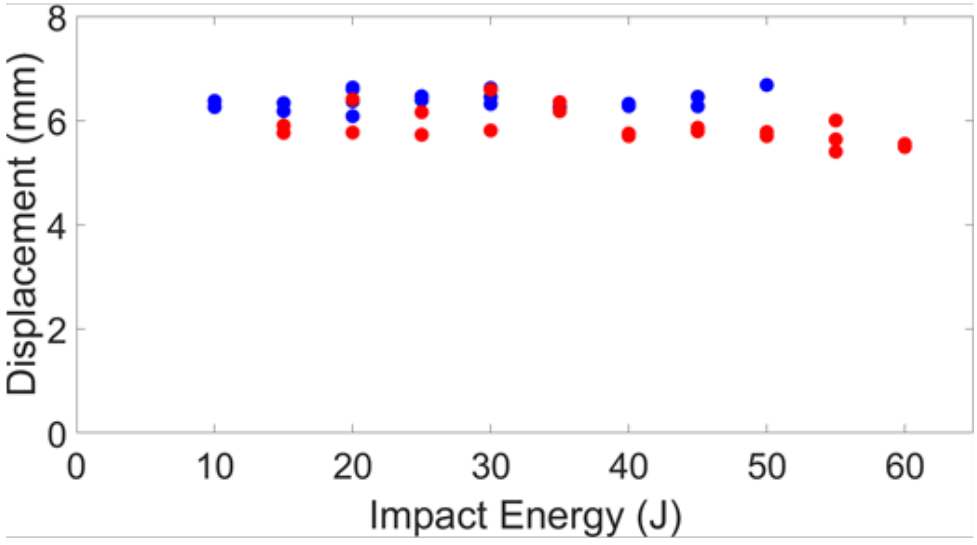

(b) Impactor displacement at first load drop

Figure 33: Load and Displacement when First Significant Load Drop is Observed

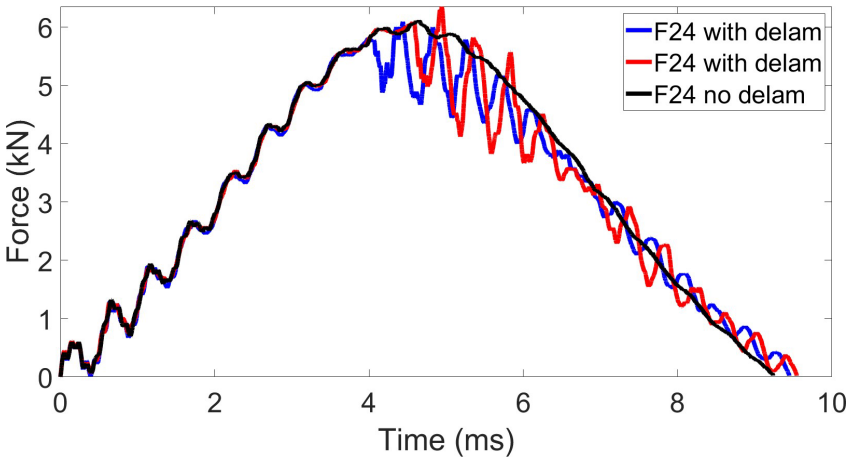

Figure 34: F24 15 J Impact Force-Time Impacts

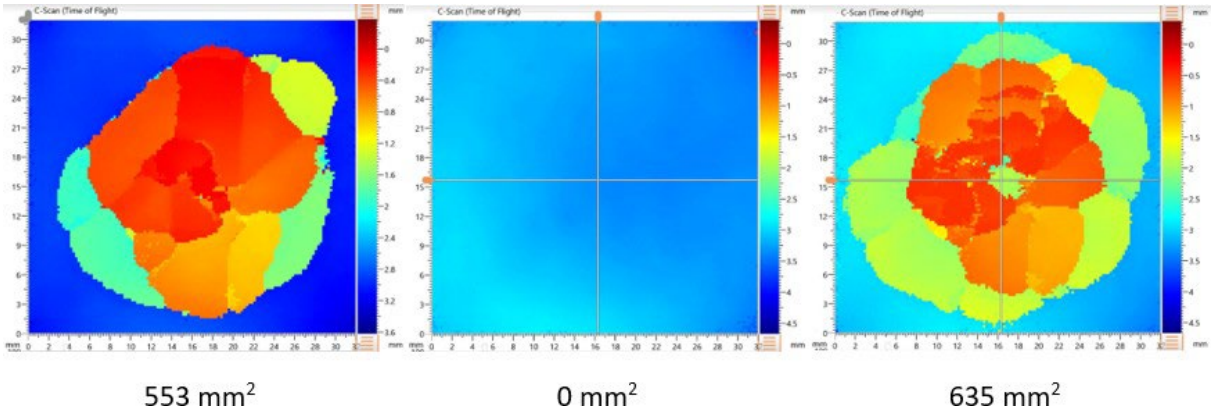

Figure 35: F24 - 15 J impact UT scans

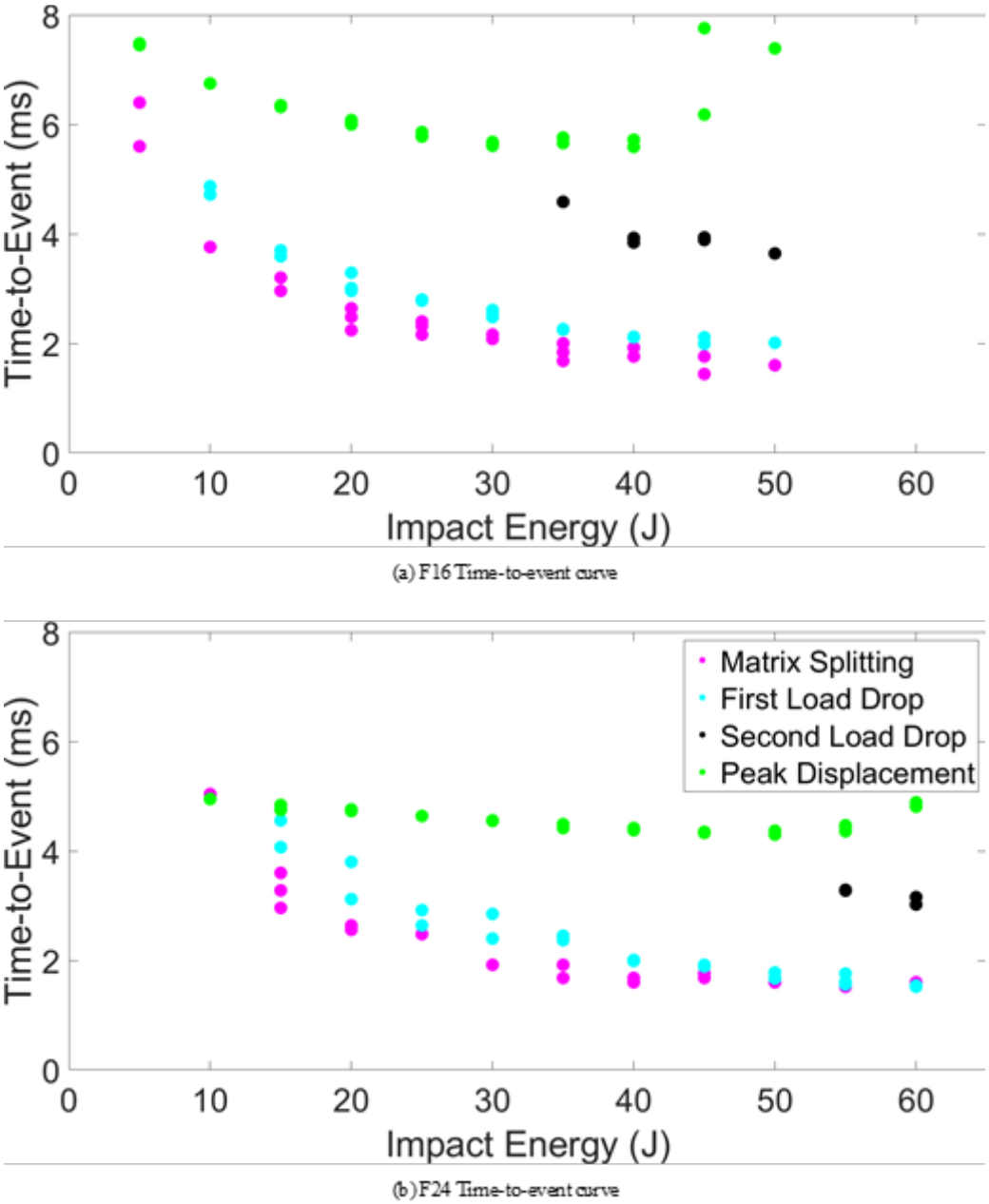

Figure 36: Time-to-event of observed failure events

4.4.2. Impact analysis – Thick composites

Figure 37 plots the similarity of the maximum displacement during the impact event of both the top and bottom surfaces. The values vary as the bottom surface maximum displacement does not account for indentation of top surface due to impactor. For each composites there is good agreement of the maximum measured displacement. The WL40 composite had the greatest displacement, followed by the WU48 composite. The WL56 composite displaced the least for a given impact energy.

Each composite shows a sharp rise in the kinetic energy loss between cases where delamination does and does not occur. This jump occurs between 15J and 20J for the WL40 composite, in which the ratio of kinetic energy loss to total prescribed energy increases from 27 percent to 57 percent. The WU48 composite experiences a similar behavior between 30J and 40J in which the energy loss ratio jumps from 37 percent to 62 percent. In the WL56 composite between 30J and 40J, the energy loss ratio increases from 40 percent to 70 percent. This behavior is shown in Figure 38.

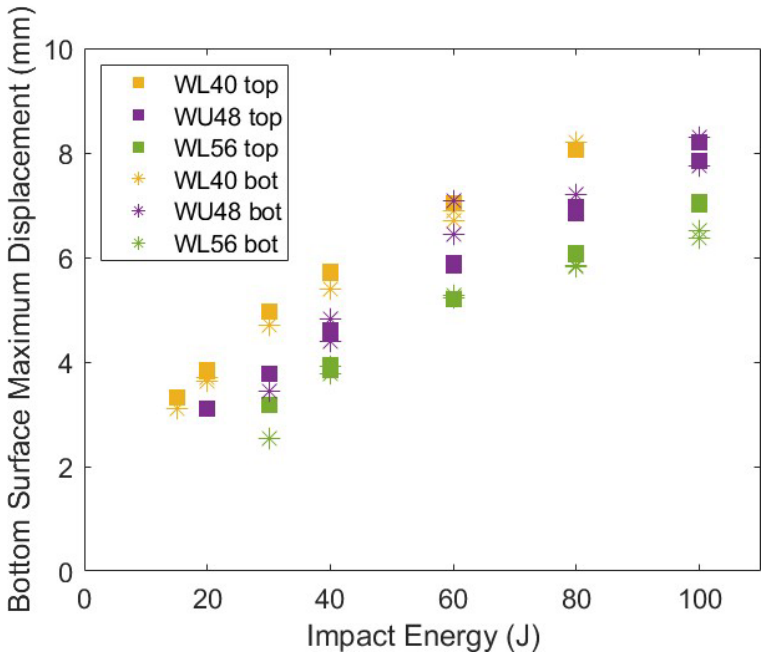

Figure 37: Top and Bottom Surface Displacement vs. Impact Energy

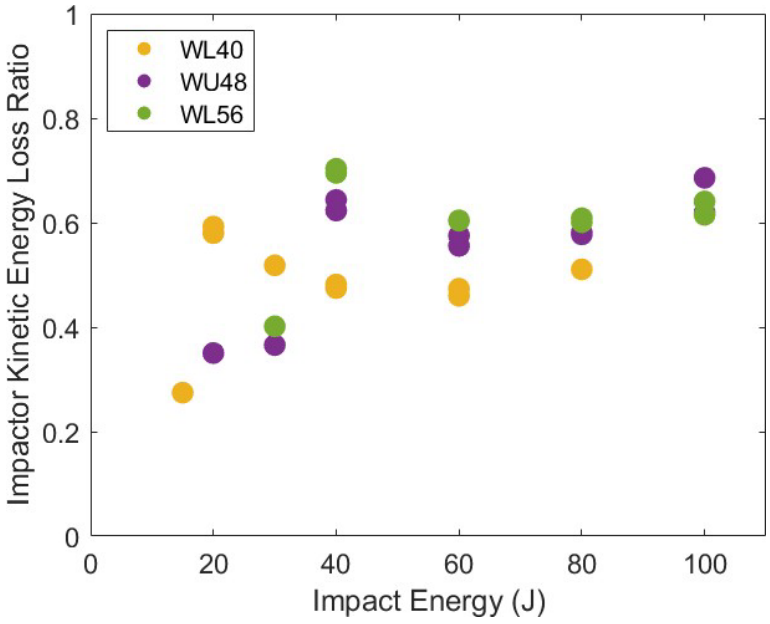

Figure 38: Kinetic Energy Loss Ratio vs. Impact Energy

4.4.3. *CAI Analysis - Thin composites*

The buckling load is plotted against the area delamination for a sample to show the strength knockdown that is observed based on the size of the delamination. Figure 39a shows the buckling load and figure 39b shows the ultimate load vs the measured area of delamination. There is no significant knockdown for the buckling load in the F16 samples, however the F24 samples start to see a slight decrease in the buckling load when the area delamination reaches 1100 mm2. From the measurement in figure 23 this area delamination in the F24 samples is expected at 39.7 J of impact energy. Both composites see a reduction in their peak load carrying capability. The F16 composite ultimate load starts to degrade at 980 mm2 which has an equivalent impact energy of 46.0 J. The F24 composite ultimate load starts to degrade at 900 mm2 which has an equivalent impact energy of 29.8 J. Figure 40 shows the stress in the loading direction for each composite at buckling initiation. The F16 composite buckles at a lower stress than the F24 composite. These results show that in all cases for non-visible impact damage on the F16 composite, there is no strength knockdown. The ultimate load of the composite starts to degrade at 46.0 J of impact energy, which is well over the BVID limit of 35 J for the F16 composite. However, this trend is different for the F24 composite. The buckling load starts to degrade at 39.7 J, and the ultimate load begins to degrade at 29.8 J. Both impact energies are beneath the BVID limit for this system.

Impacts below 55 J on the F24 ply specimen showed no signs of visible impact damage. The inability to detect the presence of impact damage on the surface of the F24 composite cannot guarantee that its ultimate compressive load will not be lowered due to the impact event.

While the CAI experiment is performed to evaluate the structural response of the test specimens, it does not aim to define a residual compressive strength of the material. Rather than discussing ultimate strength (strength is a local property usually associated with a material's ability to sustain a maximum stress [37]), it would be more appropriate to discuss the test specimen's peak load carrying capability. The compressive response of the thin laminates are affected by the out of plane displacements that may be caused by the impact damage and any other loading irregularities during the initial stages of loading. However, the load vs displacement response shows a fairly linear initial slope until the panel enters the post-buckling regime signified by a change in this slope (figure 7). As seen in figure 24, the buckling load of the test specimen is negligibly influenced by the impact energy over the given range. The ultimate failure load on the other hand, is influenced by the interaction between the damage area and the overall nonlinear deformation of the panel in the post-buckling regime. These results show that when the impact damage is small, the panels peak load carrying capacity is unaffected because it is only influenced by the size of the test specimen and the post-buckling response which drives local material failure when the local material strength is exceeded. However, as the impact damage area grows, it influences the peak load carrying capability because ultimate failure is driven by the interaction between the damage area and the overall panel deformation.

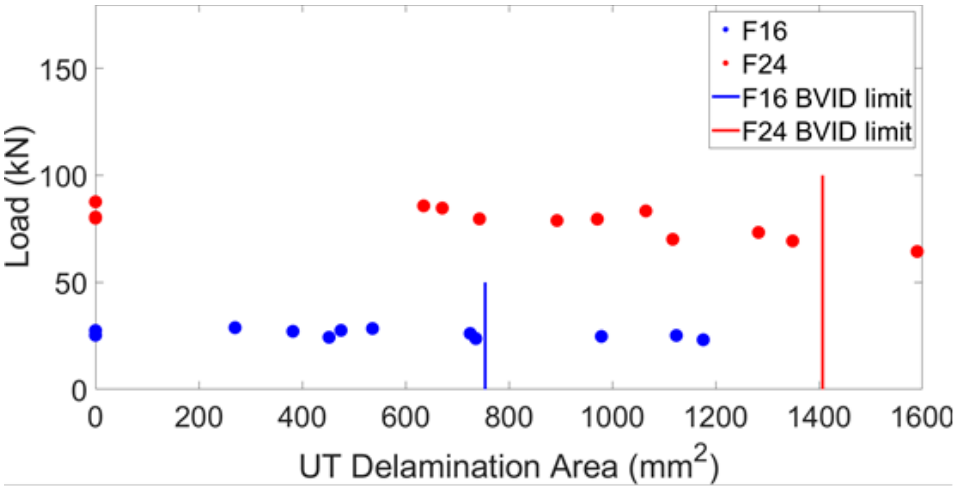

(a) Buckling load vs. UT delamination area

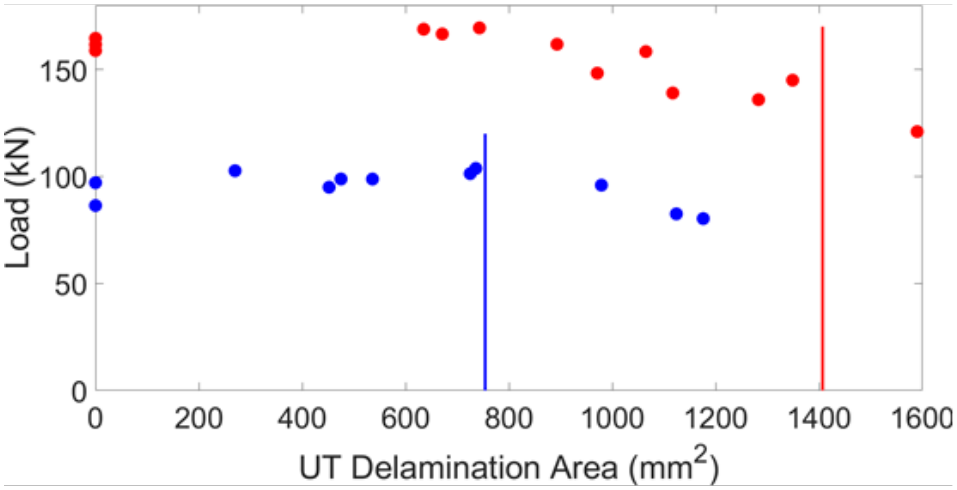

(b) Ultimate load vs. UT delamination area

Figure 39: Buckling and ultimate loads with respect to the observed delamination area

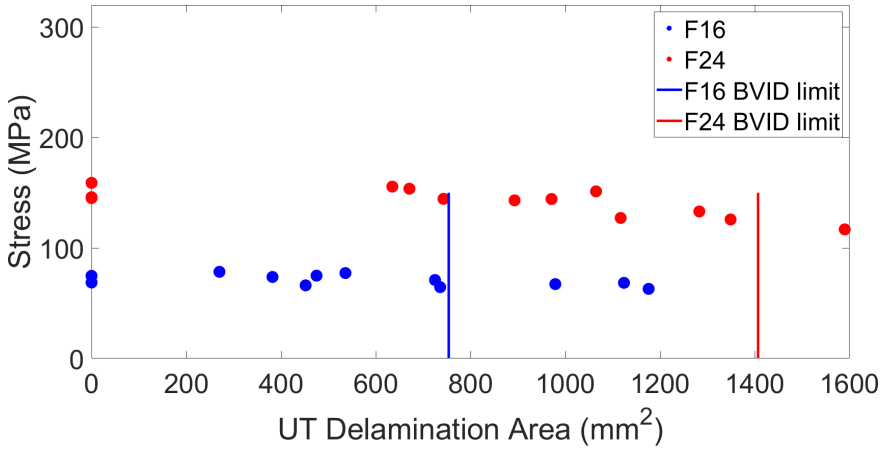

Figure 40: Stress at buckling vs. UT delamination area

4.4.4. CAI Analysis - Thick composites

Figure 41 shows the ultimate compression load of each specimen as a function of the prescribed impact energy. Figure 42 shows the ultimate compression load of each specimen as a function of the dissipated kinetic energy of the impactor.

The behavior of thick impacted composites is different than thin composites. Thinner composites experience global buckling up the sample before failure while thick composites do not. In thick samples with large delamination areas, local buckling around the location of impact can be observed, but negligibly influences the global behavior of the test specimen.

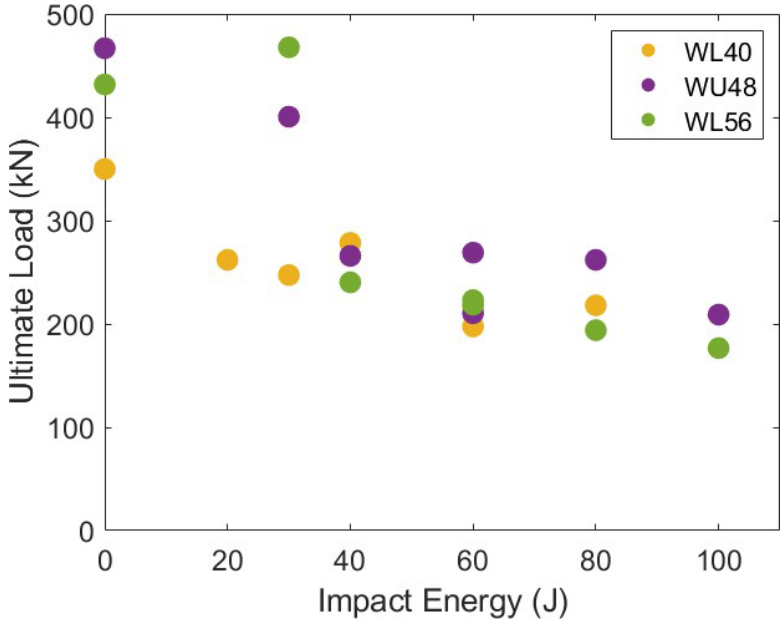

Figure 41: Ultimate Failure Load vs. Impact Energy

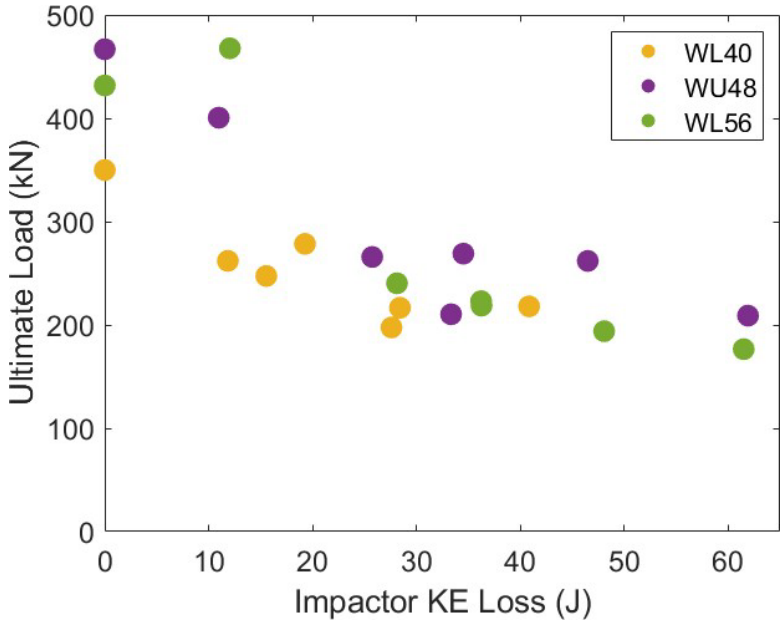

Figure 42: Ultimate Failure Load vs. Impactor Kinetic Energy Loss

4.5. Computational modeling

The experimental results shown in the previous sections illustrate the damage sequence of BVID on thin ply composites. The fact that damage events are impact energy dependent, and can be isolated, provides a rich set of data for further refining and evaluating existing mechanics based finite element models of BVID and compressive strength after impact. In this section, computational results for predicting impact damage in the 24 ply composite panels are presented. For brevity, a comprehensive presentation of computational results for all the tested panels and for predicting compressive strength after impact is relegated to a future study.

4.5.1. Modeling and mesh generation

For the impact damage modeling, the intra-ply failure is modeled using Enhanced Schapery Theory based Continuum Damage Model, [38, 39], and inter-ply failure is modeled using the cohesive contact model within the commercial finite element software package, Abaqus. Explicit analysis is conducted, without time scaling. Each simulation consists of a 178 mm by 178 mm panel with roller supports 12.4 mm from the outer edge on both the top and bottom surfaces. A hemispherical impactor is modeled to contact the center of the top surface. A finite element length of 0.5 mm (below the Bazant limit, [40]) is used, with a refined 40 mm by 40 mm mesh region centered at the location of the impactor. Impactor mass is kept constant at 8.53 kg and the velocities for each simulation are changed in order to meet a specified kinetic energy for the impactor. The supports and impactor are modeled using rigid shell elements and the composite is modeled using continuum shell elements. The study investigates a 24 ply laminate with an impact energy of 15J. The material for the composite is IM7/977-3. A set of available material properties are shown in the Appendix B.7. These properties are used in the computational model.

4.5.2. Automated BVID mesh and input file generator

A standalone input file generation tool was developed in Python scripting language, for BVID simulations. The tool models roller supports, impactor and the composite panel as per ASTM D7136 standards [1]. It has smart features that are aimed to improve simulation run times and minimize meshing errors. Two mesh regions, a fine mesh and a coarse mesh are created such that the fine mesh is positioned where significant damage is expected, in this case, directly under the impactor. The two regions are connected via a transition mesh, thereby negating the need for connecting dissimilar meshes and hence improving the simulation accuracy and run time. The tool builds a layer-by-layer mesh with each layer representing a single ply. Cohesive contact is specified automatically between each layer to model regions of delamination. Both shell and solid element can be modeled, with and without fiber aligned meshing. Boundary conditions, contact conditions, and output variables are automatically defined. Figure 43 shows an example mesh generated using the tool.

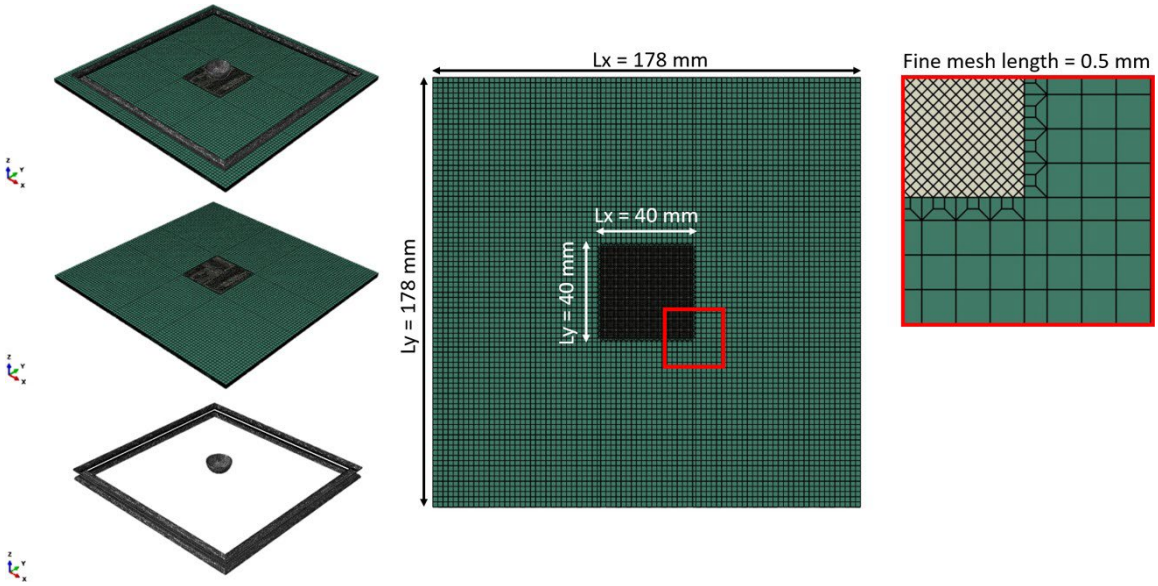

Figure 43: Left: Complete assembly of the BVID impact mesh. Right: Fine and coarse mesh region, with transition mesh connection.

4.5.3. Automated damage map extractor from BVID simulations

After a BVID simulation is conducted, the extraction of delamination, fiber damage and matrix damage maps are typically done manually and is an exceedingly time-consuming process. In this task an automated damage extraction tool was developed. The tool parses through the large simulation output database, to create a custom location coordinate based data of damage. The location-based data is ideal because it eliminates mesh dependent results, i.e.; no information of the BVID mesh is required. Therefore, making the extracted data easy to use and easy to visualize. Figure 44 shows sample output from the damage extractor tool.

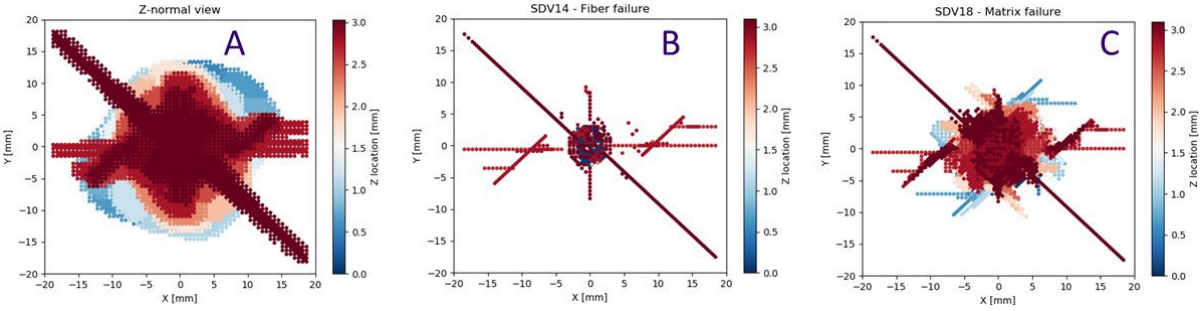

Figure 44: Overall damage pattern, A- Delamination, B- fiber damage, C – matrix damage. Colors represent the through thickness location of the damage.

4.5.4. Failure strength parameters

The computational model was implemented with the failure strength parameters shown in the Appendix B.7. However, it is known that the failure strength parameters are non-deterministic depending on a variety of factors including manufacturing process. In order to ascertain the ma-

terial failure strength parameters of the experimentally studied panels, the following process was adopted. First, the lowest impact energy where only back surface splitting was observed, with no delamination, was chosen to establish the matrix mode two failure strength, YT . Second, the lowest energy where delamination is observed was used to establish the cohesive strengths and energy release rates corresponding to the tested panels.

4.5.4.1. Matrix splitting

Tensile matrix failure was the first noticeable damage to occur in the composite and appeared on the bottom surface where splits in the matrix became visible. Direct measurement of strain from the experiment was used to establish the matrix transverse tensile strength (strain). The simulation models intralaminar fiber and matrix damage with a Hashin failure criteria. From experiments, the tensile strain on the bottom lamina (Y_T) of the F24 composite was 0.0134 when the split first initiated [41]. This direct measurement was used in the computational model.

4.5.4.2. Parameters that influence delamination

Delamination was the second significant failure event to occur after bottom surface matrix splitting. The cohesive contact modeling approach involved nine parameters to predict delamination on an interface. The nine parameters were the cohesive stiffness, the cohesive strength, and the interface toughness for the traction separation law of the cohesive interface. Each of these parameters were defined in modes 1,2, and 3. For simplicity, modes 2 and 3 were given values for each parameter. The cohesive stiffness was taken to be $1 \times 10^5 N/mm^3$ for all modes based on previous studies validating the use of this value [42]. This allowed for the stiffness of the cohesive zone to be much larger than the matrix, but not too large such that the simulation ran into numerical issues. The remaining four parameters; cohesive strength of the interface for mode 1 (σI), cohesive strength of the interface modes 2 and 3 (σII), interface mode 1 toughness (GI), and interface modes 2 and 3 toughness (GII), were established against experiment by comparing delamination size.

The choice of these four parameters using one comparison measure is difficult as the design space is large. To reduce the number of parameters, a sensitivity analysis was conducted first to identify parameters which influence the damage size the most, motivated by the study in [43].

Table 3 shows a table with the range each parameter takes on over the design space. A parameter study was conducted in order to understand the influence of the parameters on the output delamination area. A Latin Hypercube Sampling (LHS) approach was used to generate a stratified design space. A total of 40 simulations were performed to generate a refined design space for the four parameters. The baseline values for the cohesive strengths were selected based on a previously calibrated model of the same material system [44]. The interface toughness values were selected to cover a broad range of values that affected the propagation of delaminations in the model. A range of plus and minus 50 percent of the base value was applied to each parameter range. A large range enabled interpolation between outputs of the simulation to assist with adaptive sampling.

Table 3: Range of parameter values over the design space

Parameter	Minimum value	Maximum value
σ_I (MPa)	33	99
σ_{II} (MPa)	39.5	118.5
G_I (N/mm)	0.27	0.81
G_{II} (N/mm)	0.7	2.1

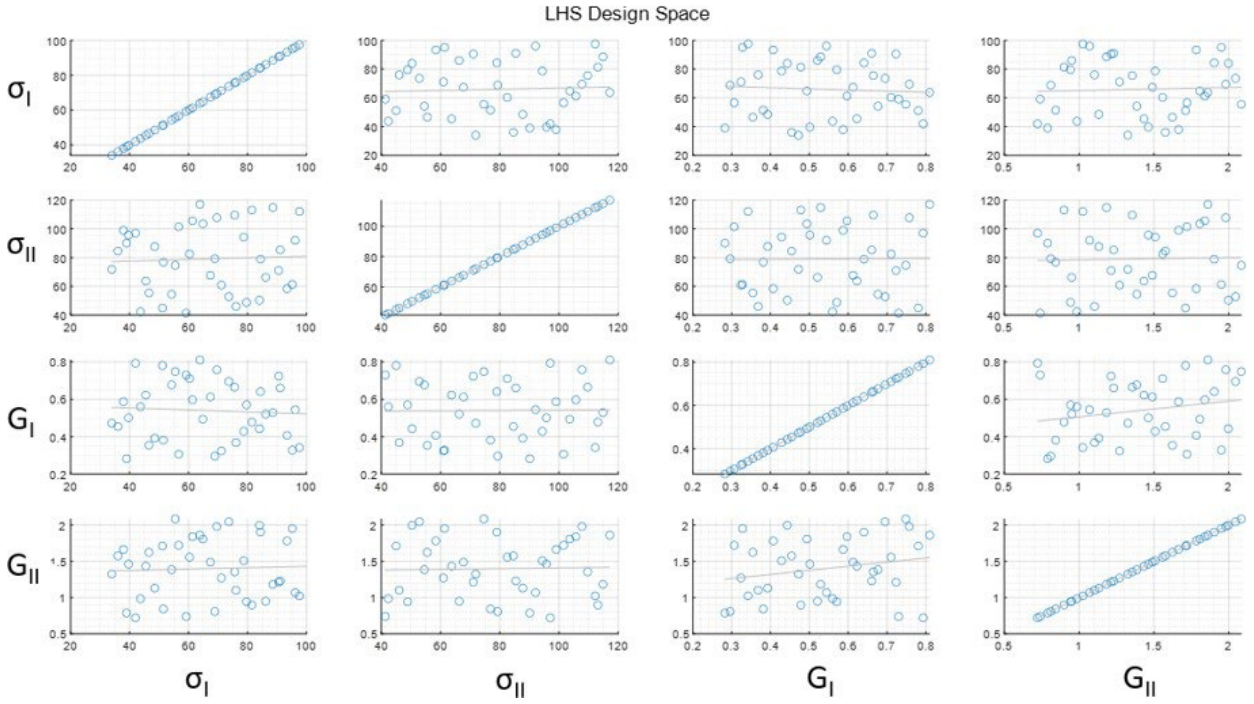

Figure 45: LHS design space for 40 test cases

Figure 45 shows an example of a stratified design space for 40 simulations. The primary diagonal represents a parameters value plotted against itself, and the off-diagonal plots show a two dimensional design space for a select pairing of parameters. A fit line is shown passing through each subplot to show the initial trend of the data for each parameter pairing. A near-horizontal fit line represents a low initial bias in the design space. LHS was selected due to its high effectiveness in representing a high-dimension and large design space.

4.5.5. *Results*

4.5.5.1. Tensile matrix failure

Figure 46 compares the computational model results (left) with an equivalent impact experiment (right) at 15J [41]. These images are centered on the bottom surface of the composite. The

simulated damage is shown in blue, while the intact matrix is shown in red. The right image outlines a split in the matrix on the bottom surface of an experimental result. The matrix splits are outlined in blue in the experimental image for ease of identification and comparison. The simulation predicted a split length of 13 mm (0.512”) while the experimental split measurement was 15.8 mm (0.625”). The time at which back splitting initiated in the experiment was 4.20 ms [41]. The model predicts the initiation of matrix splitting at 3.15 ms. The model under predicts the total length of the matrix split by 18 percent and under predicts the time until the matrix split by 25 percent. Adjusting parameters of the model to fit one of these criteria causes a larger deviation in the other.

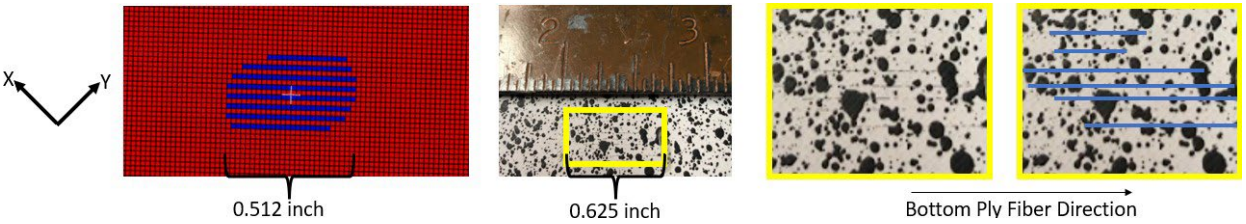

Figure 46: Matrix splitting compared between experimental and simulated results

4.5.5.2. Delamination

The results from the parameter study were analyzed using the Nodeworks, [45] sensitivity analysis toolbox. The primary output of the analysis was the UT scan area equivalent of the delamination area (A). The simulated scan was taken as a top-down view on the delamination from the perspective of the impacted surface. A second-order polynomial was selected to fit the output from the parameter study. A response surface was generated based on the polynomial fit and is shown in figure 47. The multidimensional design space cannot be plotted, hence for simplicity the response surface output is shown with respect to two of the input parameters. Blue markers represent the delamination area outputs for a specific combination of input parameters. Figure 47 shows the output value plotted against the cohesive mode 2,3 strength and the interface mode 2,3 toughness. The transparent red surface represents the predictive polynomial fit with an R2 value.

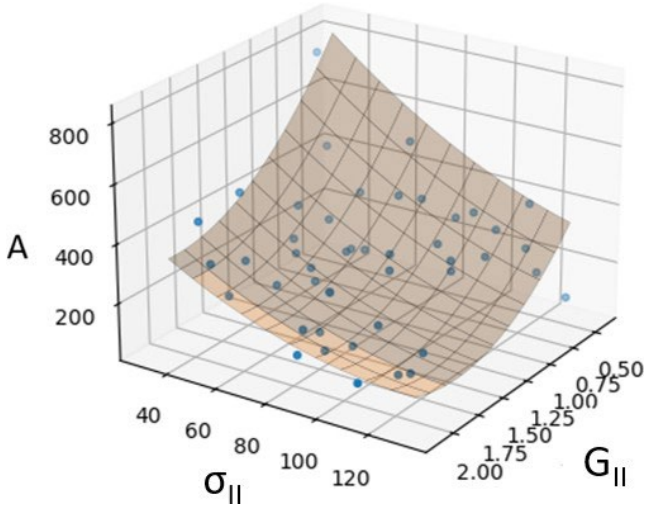

Figure 47: Response surface

A global sensitivity analysis calculated the sensitivity of each input parameter using the Sobol method. The sensitivity of the output based on each input parameter is described in figure 48. The delamination area is driven by the mode 2,3 cohesive strength and the interface mode 2,3 toughness. It is equally important that the mode 1 cohesive strength and interface toughness have little influence on the output delamination area. The first order sensitivities are tabulated in figure 48b to quantify the influence each input parameters has on the output. Figure 48a also shows that there is little cross-correlation or second order sensitivities that influence the output of the model. A general optimizer within Nodeworks was used to perform adaptive sampling on the original design space. Using the known delamination area of the experimental results (603mm2) and the discovered sensitivities of each input parameter from figure 48, the optimizer produced combinations of input parameters that match the desired output [41]. The solutions from the optimization served as a Pareto front. Several combinations of parameters led to possible matches and serve as baseline for subsequent iterations of adaptive sampling.

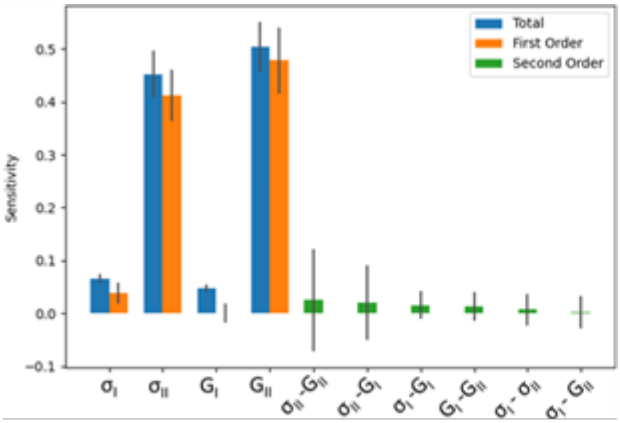

(a) Overall sensitivities

	Sensitivity	Confidence
σ_I	0.0386	0.0194
σ_{II}	0.412	0.0489
G_I	0.000429	0.0183
G_{II}	0.478	0.0625

(b) First order sensitivities

Figure 48: Cohesive parameter sensitivities

Table 4 : Final cohesive paramters

Parameter	Final value
σ_I (MPa)	56
σ_{II} (MPa)	70
G_I (N/mm)	0.178
G_{II} (N/mm)	0.612

Adaptive sampling centered around these values generated a refined output response in a smaller design space. After several iterations of input parameter combinations, the final cohesive parameters were determined. The final value for each parameter are shown in table 4. Interface toughness GI was fixed at 0.178 N/mm based on AFRL experimental results listed in Appendix B. As shown in figure 48, GI has little correlation with the output delamination area and did not

need to be solved numerically. With these final parameter values, the resulting delamination area predicted was 7 percent below the average of the experimental results at 15 J.

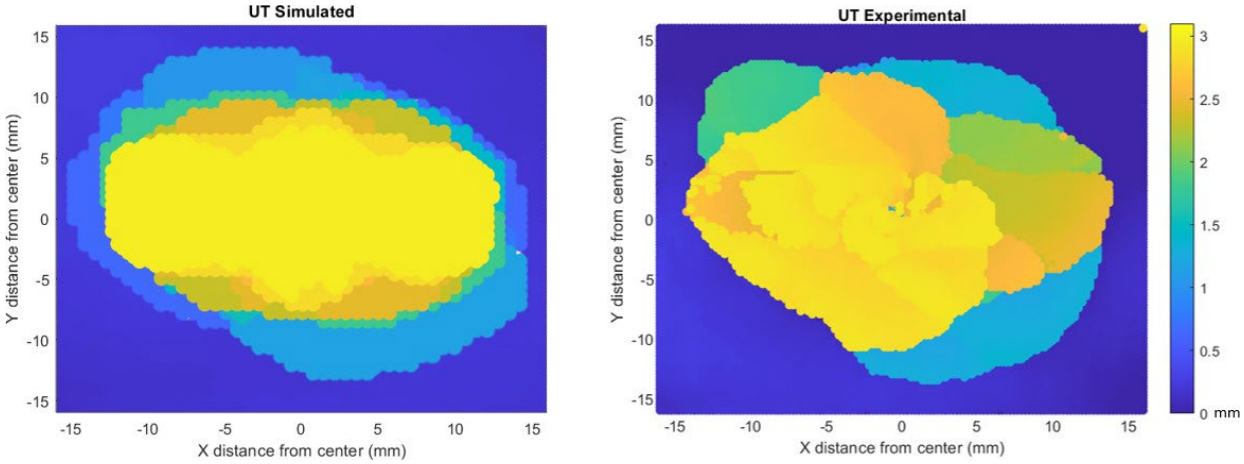

Figure 49: Comparison between simulation (left) and experimental (right) delamination patterns

A comparison between simulated and experimental UT delamination areas are shown for the 15J impact in figure 49. The delamination patterns and shape match well. Each delamination plot is centered beneath the point of impact as is displayed in a 32mm by 32mm region. A color bar on the right side provides the height through the thickness where delamination is first present. The yellow regions are located close to the impacted or top surface of the composite while the dark blue represents the bottom surface of the composite at a height of 0 mm.

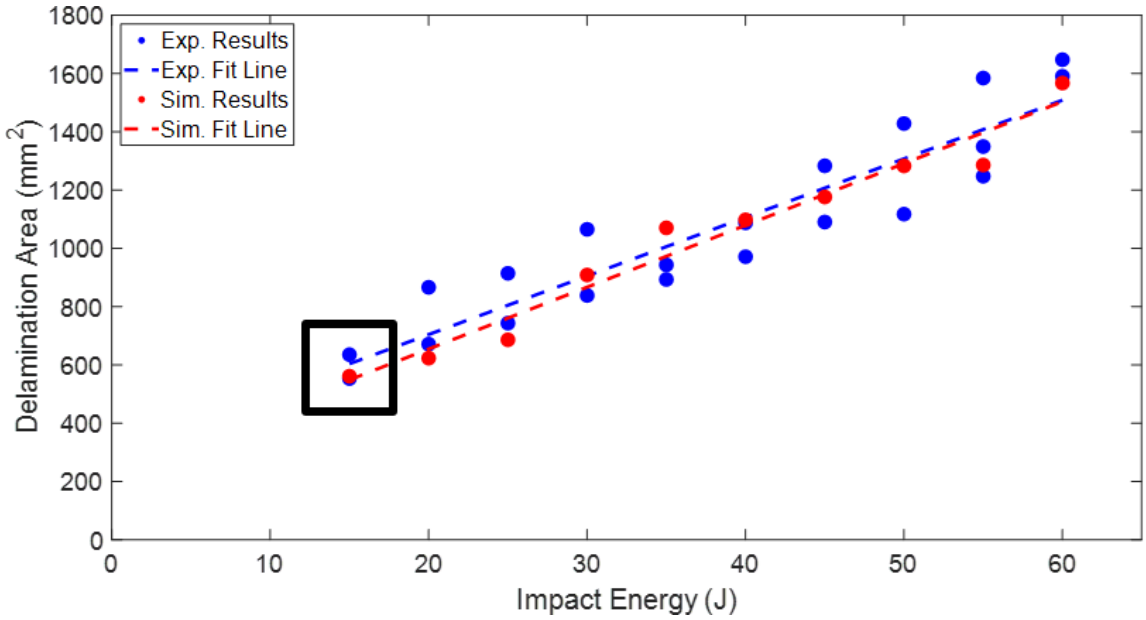

Figure 50 : Experimental result and simulated prediction of delamination area for BVID

With the input parameters finalized as accurate for the 15 J case, additional simulations were run at 5 J intervals up to 60 J. The black box region in figure 50 indicates where the parameter calibration was performed. With the same set of cohesive parameters, the simulated area of delamination was accurately predicted over the full range of BVID energies shown in figure 50. A

linear fit line represents the trend line for both the experimental results and the simulated prediction. The equation for the experimental fit line is Y = 20.1X + 302. The equation for the simulated fit line is Y = 21.2X + 230, in which Y represents the delamination area and X represents the impact energy. The simulation slightly under predicts the delamination area at each energy. The simulation idealized a pristine and symmetric case, while the experimental results are more likely to incur additional damage through minor defects in the composite.

It is also important to recognize the effect the cohesive parameters have on other aspects of the model. A primary goal of the model is to match the force-time response of the impactor. Figure 51 shows the simulation with the smallest delamination area 90mm2 (in red) and largest delamination area 508mm2 (in blue) from the initial set of 40 simulations performed. The response curves are very similar and include a maximum load difference of 0.28 kN which is 3.8 percent of the larger maximum load. The cohesive parameters for Sim27 are: σI = 71.4 MPa, σII = 45.0 MPa, GI = 0.496 N/mm, GII = 0.826 N/mm. The cohesive parameters for Sim35 are: σI = 74.5 MPa, σII = 117 MPa, GI = 0.274 N/mm, GII = 1.79 N/mm. In these extreme instances, the mode 2,3 cohesive strength and interface toughness values (the most sensitive parameters) are near opposite ends of the design space. This provides confidence that changes to the cohesive parameters have little effect on the global force - time response and that changing the parameters does not alter this.

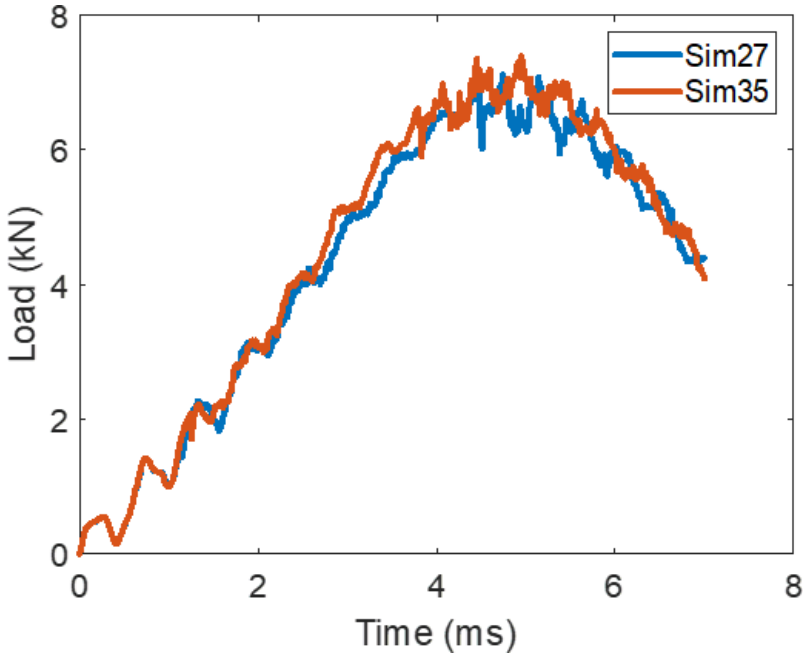

Figure 51: Impact Force-Time response

Table 5 shows a comparison of four data sets for the IM7/977-3 material system including the optimized set of values determined by the experimental data presented in this report. It is noted that in this table, we provide in the fifth column the ratio of computed delamination area footprint to the scanned (ultrasonically, UT) delamination area footprint. The other two columns provide the computed total delamination area, labeled as Full Area (sum of the areas of every interface that has delaminated) as well as the interface with the largest delamination area, as computed. Using the UT scan, it is not possible to measure the delaminated areas of each interface due to shadowing,

however, these areas can be computed. With the UT scan, the total footprint can be measured and this was used as a metric to determine the best set of parameters.

As seen in the fifth column of that table (labelled UT Sim/Exp), the predicted delamination area footprint when compared against the corresponding experimental measurements are within 7% percent of each other lending credence to the inverse modeling method adopted to determine the failure strength and toughness parameters.

Table 5: IM7/977-3 sets of cohesive parameters and prediction for 15J impact

Parameter	σ_I	σ_{II}	G_I	G_{II}	UT Sim/Exp	Full Area	Largest Interface
Zhang et al. [46]	64	121	0.32	0.58	0.302	$1848mm^2$	$N = 12, A_N = 166mm^2$
AFRL tests	77.3	118	0.178	0.62	0.443	$1850mm^2$	$N = 14, A_N = 232mm^2$
Lin et al. [3]	64	79	0.255	0.896	0.609	$4635mm^2$	$N = 6, A_N = 395mm^2$
Nodeworks Model	56	70	0.178	0.612	0.931	$6545mm^2$	$N = 5, A_N = 526mm^2$

5. CONCLUSIONS

This report illustrates the significant differences of BVID for thin and thick composites structures that are earmarked for future airframe applications. It is shown that a severe knockdown in compressive load carrying capability occurs in thick composites that is vastly different than thin composites. This is because during impact, the thicker composites experience less out of plane deformation as a result of their bending stiffness (duo to the stacking sequence and overall thickness). This results in higher shear stresses between lamina producing delaminations that are much larger than what is seen in thin composites at equivalent energies.

In the CAI experiment, the thin composites buckle before reaching ultimate failure, while the thick composites do not. The thin composites failure is driven by the geometry of the buckled configuration, the damage sustained from impact, and the compressive load. The thick composites failure is only driven by the latter two.

The following conclusions are made:

- The F16 composite experiences delamination without visible damage between impact energies of 10 J to 35 J. The F24 composite experiences delamination without visible impact damage between impact energies of 15 J to 55 J.
- The first significant load drop in the response represents delamination initiation for the studied composites. A change in the load signal frequency occurs once delamination initiates. The initiation of back splitting is not associated with the load drop for the 16 and 24 ply composites.
- The thinner samples (F16) experience matrix splitting on the back surface first, delamination next, and only in high-energy cases do they produce top surface fiber compressive failure. The matrix splitting and delamination occur at closer times in the 24 ply composites. At higher impact energies, the order of these failure events start to intersect.

- Compressive fiber failure on the top surface of the composite causes the dent depth to exceed the BVID limit. The top surface failure also releases a large amount of energy, which reduces the impactors' kinetic energy.
- The fit lines shown in Figure 17 allow for a quantitative relationship to connect the ultra-sound delamination footprint area to impact energy. The F24 composite consistently experiences larger detected delamination areas relative to the F16 composite.
- Both the F16 and F24 composite panels buckle before reaching their ultimate failure in the compression after impact study.
- CAI knockdown in peak load carrying capability is not observed in the F16 samples below the BVID limit.
- CAI knockdown in peak load carrying capability is observed in the F24 samples starting at 30 J which corresponds to an UT delamination footprint area of $980 mm^2$. This means that there is a strength knockdown in the composite before any impacted surface damage is visible.
- The detailed experimental results provide a unique set of data for the dominant failure modes in impact and CAI. These can be used to establish difficult to measure interface parameters for a computational model with good confidence.
- The thin composites (16 and 24 ply) produce both BVID and VID across the range of impact energies tested. A clear BVID impact energy is defined for each laminate.
- The thick composites produced BVID for all of the tested impact energies.
- The thin composites did not suffer severe ultimate load knockdowns, but a decrease in the load carrying capability was observed in the F24 composite before damage was determined to be visible. The F16 composite only began to experience ultimate load knockdown after impact damage was already visible.
- The thick composites suffered large ultimate load knockdown once impact induced delamination was present. The onset of delamination is very sudden and the size of the delamination is much larger than what is observed in thin composites.
- Thin composites buckled in the CAI experiment before reaching ultimate failure. Thick composites reached ultimate failure before the onset of buckling.

A single definition for BVID does not adequately represent the compressive behavior of composites after impact. This report shows that for some composites, visible impact damage can produce little to no effect on the compressive load carrying capability while other composites can experience up to a 60 percent decrease in their ultimate compressive load without any visually detected damage

6. ACKNOWLEDGEMENTS

The authors are grateful for the financial support and for the material for the program, from the Air Force Research Lab (AFRL) through the Structural Integrity Research Collaborations for Aircraft (SIRCA) program. This material is based on research sponsored by the U.S. Air Force under agreement number FA8650-19-2-2213.

7. DISCLAIMER

REFERENCES

[1] Standard test method for measuring the damage resistance of a fiber-reinforced polymer matrix composite to a drop-weight impact event, ASTM Standard D7136 (2009).

[2] H. Chai, W. Knauss, C. Babcock, Observation of damage growth in compressively loaded laminates, Experi- mental Mechanics 23 (1983) 329–337.

[3] S. Lin, V. Ranatunga, A. M. Waas, A comprehensive experimental and computational study on lvi induced damage of laminated composites, in: AIAA Scitech 2021 Forum, 2021, p. 1623.

[4] S. Lin, A. M. Waas, The effect of stacking sequence on the lvi damage of laminated composites; experiments and analysis, Composites Part A: Applied Science and Manufacturing 145 (2021) 106377.

[5] M. Flores, D. Mollenhauer, V. Runatunga, T. Beberniss, D. Rapking, M. Pankow, High-speed 3d digital image correlation of low-velocity impacts on composite plates, Composites Part B: Engineering 131 (2017) 153–164.

[6] M. Waas, S. I. Thorsson, M. Rassaian, Prediction of low-velocity face-on impact response and com- pression after impact (cai) of composite laminates using est and cohesive modeling (dczm), in: 2018 AIAA/ASCE/AHS/ASC Structures, Structural Dynamics, and Materials Conference, 2018, p. 1704.

[7] M. Pankow, B. Justusson, A. M. Waas, Three-dimensional digital image correlation technique using sin- gle high-speed camera for measuring large out-of-plane displacements at high framing rates, Appl. Opt. 49 (2010) 3418–3427. URL: http://www.osapublishing.org/ao/abstract.cfm?URI=ao-49-17-3418. doi:10.1364/AO.49.003418.

[8] J. H. Heida, D. J. Platenkamp, Evaluation of non-destructive inspection methods for composite aerospace structures, in: International Workshop of NDT Experts, volume 10, 2011, p. 12.

[9] C. Garnier, M.-L. Pastor, F. Eyma, B. Lorrain, The detection of aeronautical defects in situ on composite structures using non destructive testing, Composite structures 93 (2011) 1328–1336.

[10] Pelivanov, T. Buma, J. Xia, C.-W. Wei, M. O'Donnell, Ndt of fiber-reinforced composites with a new fiber- optic pump–probe laser-ultrasound system, Photoacoustics 2 (2014) 63–74.

[11] Carbon-fibre-reinforced plastics — Determination of compression-after-impact properties at a specified impact- energy level, Technical Report ISO 18352:2009, 2009.

[12] R. Talreja, N. Phan, Assessment of damage tolerance approaches for composite aircraft with focus on barely visible impact damage, Composite Structures 219 (2019) 1–7.

[13] M. S. Rajput, Experimental and numerical study of the response to various impact energy levels for composite sandwich plates with different face thicknesses, Journal of Sandwich Structures Materials (2019).

[14] L. S. Kistler, A. M. Waas, On the response of curved laminated panels subjected to transverse impact loads, International journal of solids and structures 36 (1999) 1311–1327.

[15] S. Lin, S. I. Thorsson, A. M. Waas, Predicting the low velocity impact damage of a quasi-isotropic laminate using est, Composite Structures 251 (2020) 112530. URL: https://www.sciencedirect.com/science/ article/pii/S026382232030492X. doi:https://doi.org/10.1016/j.compstruct.2020.112530.

[16] S. I. Thorsson, A. M. Waas, M. Rassaian, Low-velocity impact predictions of composite laminates using a continuum shell based modeling approach part a: Impact study, International Journal of Solids and Structures 155 (2018) 185–200.

[17] P. J. Falzon, I. Herszberg, Prediction of the compression-after-impact strength of 2-d braided composites, in: Proc. 11th Int. Conf. on Composite Materials, volume 5, 1997, pp. 307–316.

[18] G. Davies, R. Olsson, Impact on composite structures, The Aeronautical Journal 108 (2004) 541–563. Standard test method for compressive residual strength properties of damaged polymer matrix composite plates, ASTM Standard D7137 (2012).

[19] S. Sanchez-Saez, E. Barbero, R. Zaera, C. Navarro, Compression after impact of thin composite laminates, Com- posites Science and Technology 65 (2005) 1911–1919. doi:https://doi.org/10.1016/j.compscitech. 2005.04.009.

[20] M. de Freitas, L. Reis, Failure mechanisms on composite specimens subjected to compression after im- pact, Composite Structures 42 (1998) 365–373. URL: https://www.sciencedirect.com/science/ article/pii/S0263822398000816. doi:https://doi.org/10.1016/S0263-8223(98)00081-6, interna- tional Workshop on Experimental Techniques in the Analysis of Composite Structures.

[21] V. Hawyes, P. Curtis, C. Soutis, Effect of impact damage on the compressive response of com- posite laminates, Composites Part A: Applied Science and Manufacturing 32 (2001) 1263–1270. URL: https://www.sciencedirect.com/science/article/pii/S1359835X01000720. doi:https://doi.org/10.1016/S1359-835X(01)00072-0.

A. Duarte, I. Herszberg, R. Paton, Impact resistance and tolerance of interleaved tape laminates, Composite structures 47 (1999) 753–758.

[22] G. Dorey, S. Bishop, P. Curtis, On the impact performance of carbon fibre laminates with epoxy and peek matrices, Composites Science and Technology 23 (1985) 221–237.

[23] S. M. Bishop, The mechanical performance and impact behaviour of carbon-fibre reinforced peek, Composite structures 3 (1985) 295–318.

[24] S. Lin, A. M. Waas, An Experimental and Computational Study on the Low Velocity Impact-Induced Damage of a Highly Anisotropic Laminated Composite Panel, Journal of Applied Mechanics 88 (2021). doi:10.1115/ 1.4050619.

[25] S. Takeda, S. Minakuchi, Y. Okabe, N. Takeda, Delamination monitoring of laminated composites subjected to low-velocity impact using small-diameter fbg sensors, Composites Part A: Applied Science and Manufacturing 36 (2005) 903–908.

[26] S. Rivallant, C. Bouvet, E. Abi Abdallah, B. Broll, J.-J. Barrau, Experimental analysis of cfrp laminates sub- jected to compression after impact: The role of impact-induced cracks in failure, Composite Structures 111 (2014) 147–157.

[27] S. Basu, A. M. Waas, D. R. Ambur, Prediction of progressive failure in multidirectional composite laminated panels, International Journal of Solids and Structures 44 (2007) 2648–2676.

[28] M. Ebina, A. Yoshimura, K. Sakaue, A. M. Waas, High fidelity simulation of low velocity impact behavior of cfrp laminate, Composites Part A: Applied Science and Manufacturing 113 (2018) 166–179.

[29] N. Hongkarnjanakul, C. Bouvet, S. Rivallant, Validation of low velocity impact modelling on different stacking sequences of cfrp laminates and influence of fibre failure, Composite Structures 106 (2013) 549–559.

[30] W. Tan, B. G. Falzon, L. N. Chiu, M. Price, Predicting low velocity impact damage and compression-after- impact (cai) behaviour of composite laminates, Composites Part A: Applied Science and Manufacturing 71 (2015) 212–226.

[31] S. I. Thorsson, A. M. Waas, M. Rassaian, Low-velocity impact predictions of composite laminates using a continuum shell based modeling approach part b: Bvid impact and compression after impact, International Journal of Solids and Structures 155 (2018) 201–212.

[32] C. Bouvet, S. Rivallant, J.-J. Barrau, Low velocity impact modeling in composite laminates capturing permanent indentation, Composites Science and Technology 72 (2012) 1977–1988.

[33] Y. Shi, T. Swait, C. Soutis, Modelling damage evolution in composite laminates subjected to low velocity impact, Composite Structures 94 (2012) 2902–2913.
[34] J. H. Yu, P. G. Dehmer, Dynamic impact deformation analysis using high-speed cameras and aramis photogram- metry software, Army Research Laboratory (2010).
[35] R. Talreja, A. M. Waas, Concepts and definitions related to mechanical behavior of fiber reinforced composite materials, Composites Science and Technology 217 (2022) 109081. URL: https://www. sciencedirect.com/science/article/pii/S0266353821004371. doi:https://doi.org/10.1016/j. compscitech.2021.109081.
[36] P. Davidson, E. J. Pineda, C. Henrich, A. M. Waas, A unified model for predicting the open hole tensile and com- pressive strengths of composite laminates for aerospace applications, in: 54th AIAA/ASME/ASCE/AHS/ASC structures, structural dynamics, and materials conference, 2013, p. 1613.
[37] E. J. Pineda, A. M. Waas, Numerical implementation of a multiple-isv thermodynamically-based work poten- tial theory for modeling progressive damage and failure in fiber-reinforced laminates, International journal of fracture 182 (2013) 93–122.
[38] Z. P. Bazˇant, B. H. Oh, Crack band theory for fracture of concrete, Mate´riaux et construction 16 (1983) 155–177. Seamone, Andrew and Waas, Anthony M. and Davidson, Paul, Experimental analysis of low velocity impact near the bvid limit on carbon fiber reinforced polymer panels, in: ASC Thirty-Sixth Technical Conference, 2021. doi:10.12783/asc36/35807.
[39] Jablo´nski, Lukasz, Halicka, Anna, Influence of surface based cohesive parameters on static performance of concrete composite t-shaped beams, MATEC Web Conf. 262 (2019) 08003. URL: https://doi.org/10. 1051/matecconf/201926208003. doi:10.1051/matecconf/201926208003.
[40] P. A. Gustafson, A. M. Waas, The influence of adhesive constitutive parameters in cohesive zone finite element models of adhesively bonded joints, International Journal of Solids and Structures 46 (2009) 2201–2215.
[41] S. Lin, A. M. Waas, Experimental and high-fidelity computational investigations on the low velocity impact damage of laminated composite materials, in: AIAA Scitech 2020 Forum, 2020, p. 0724.
[42] U.S. Department of Energy National Energy Technology Laboratory, Nodeworks, http://mfix.netl.doe. gov/nodeworks, 2021. Accessed: 2021-07-07.
[43] J. Zhang, X. Zhang, An efficient approach for predicting low-velocity impact force and damage in composite laminates, Composite Structures 130 (2015) 85–94.
[44]M. J. Bogdanor, C. Oskay, Prediction of progressive damage and strength of im7/977-3 composites using the eigendeformation-based homogenization approach: Static loading, Journal of Composite Materials 51 (2017) 1455–1472.

APPENDIX A: MATERIAL PROPERTIES

Table 6: : IM7/977-3 Material Properties

Variable	Description	Value	Source
ρ	Density	$1.5 * 10^{-9}$ t/mm^3	[3]
E_1	1-direction modulus	164.3 GPa	[47]
E_2	2-direction modulus	8.840 GPa	[47]
G_{12}	Shear modulus	6.735 GPa	[3]
ν_{12}	Poisson ratio	0.329	AFRL tests
X_T	Lamina 1-direction initiation strain (T)	0.0171	[3]
X_C	Lamina 1-direction initiation strain (C)	0.0112	[3]
Y_T	Lamina 2-direction initiation strain (T)	0.0134	[41]
Y_C	Lamina 2-direction initiation strain (C)	0.0279	[3]
Z_{12}	Shear initiation strain	0.059	[3]
k_I	Cohesive stiffness mode I	$1 * 10^5$ N/mm^3	[42]
k_{II}	Cohesive stiffness mode II	$1 * 10^5$ N/mm^3	[42]
σ_I	Cohesive strength mode I	56 MPa	Inverse modeled
σ_{II}	Cohesive strength mode II	70 MPa	Inverse modeled
G_I	Interface toughness mode I	0.178 N/mm	AFRL tests
G_{II}	Interface toughness mode II	0.612 N/mm	Inverse modeled

APPENDIX B: CLASSICAL LAMINATION THEORY COMPOSITE STIFFNESS PREDICTION

Table 7 : IM7/977-3 stiffness prediction

Variable	Description	Value	Source
E_1	1-direction modulus	164.3 GPa	[47]
E_2	2-direction modulus	8.840 GPa	[47]
G_{12}	Shear modulus	6.735 GPa	[3]
ν_{12}	Poisson ratio	0.329	AFRL tests

APPENDIX C: IMPACT FORCE-TIME RESPONSE AT MULTIPLE ENERGIES

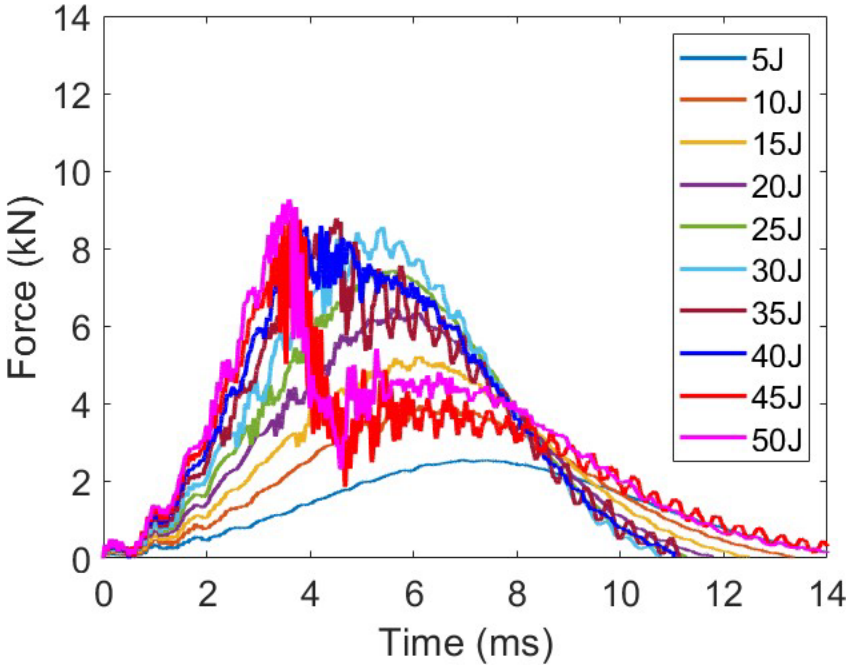

Figure 52: F16 force-time response

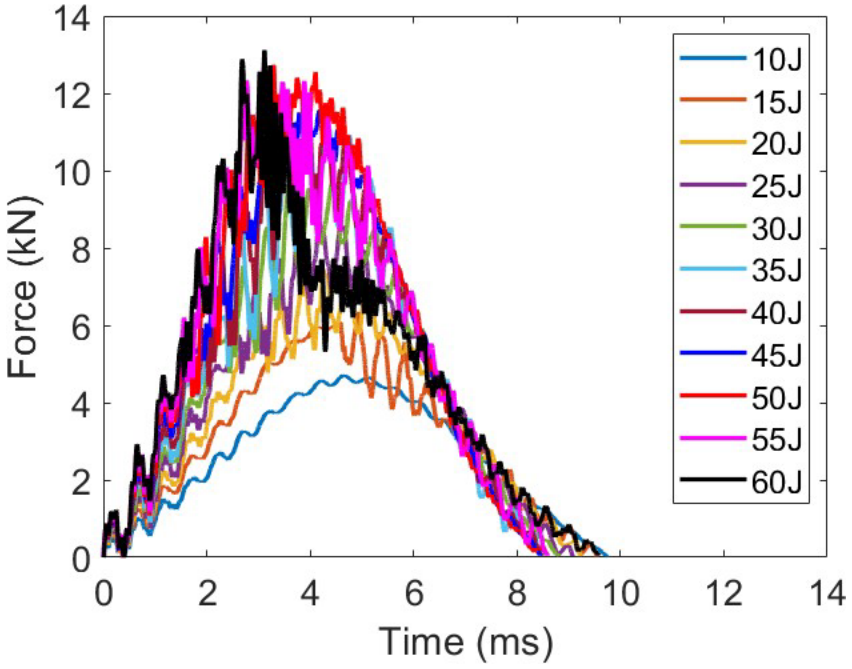

Figure 53: F24 force-time response

APPENDIX A: LIST OF PUBLICATIONS

- Seamone, Andrew, et al. ”Low velocity impact and compressive response after impact of thin carbon fiber composite panels.” International Journal of Solids and Structures (2022): 111604.
- Seamone, Andrew, Anthony M. Waas, and Paul Davidson. ”Experimental Analysis of Low Velocity Impact on Carbon Fiber Reinforced Polymer (CFRP) Composite Panels.” AIAA SCITECH 2022 Forum. 2022.
- Seamone, Andrew, et al. ”Influence of input parameters on Barely Visible Impact Damage (BVID) simulation.” AIAA SCITECH 2022 Forum. 2022.
- Seamone, Andrew, et al. ”Experimental analysis of low velocity impact near the bvid limit on carbon fiber reinforced polymer panels.” Proceedings of the American Society for Composites—Thirty-Sixth Technical Conference on Composite Materials. 2021.
- Lu, D., Davidson, P., Waas, A. M., Ranatunga, V. (2021). On the estimation of ply-by-ply information from UT scan of impacted composite panel. In AIAA Scitech 2021 Forum (p. 1510).